RECONSTRUCTING HYDRODYNAMIC FLOW PARAMETERS OF THE 1700 TSUNAMI AT ECOLA CREEK, CANNON BEACH, OREGON

Final Technical Report

U.S. Geological Survey Award No. 07HQGR0089

August 2008

By

Robert C. Witter[1], Yinglong Zhang[2] and George Priest[1]

[1]Oregon Dept. of Geology and Mineral Industries, Coastal Field Office, 313 SW 2nd, Suite D, Newport, Oregon 97365

[2]OGI School of Science and Engineering, Oregon Health & Science University, 20000 NW Walker Road, Beaverton, OR 97006

ABSTRACT

Coastal communities in the western U.S. face risks of inundation by distant tsunamis that travel across the Pacific Ocean as well as local tsunamis produced by great (M >8) earthquakes on the Cascadia subduction zone. In 1964 the M 9.2 Alaska earthquake generated a distant tsunami that flooded Cannon Beach, a small community (population 1640) in northwestern Oregon, causing over $230,000 in damages. However, in the wake of the 2004 Indian Ocean tsunami, renewed concern about the potential impacts of a local Cascadia tsunami, has motivated a need for closer examination of the hazard. This study applies a simple sediment transport model to reconstruct the flow speed of the most recent Cascadia tsunami that flooded the region in 1700 using the thickness and grain size of sand layers deposited by the waves. Sand sheets recording the 1700 tsunami were sampled in the field and analyzed in the laboratory to produce model inputs. TsuSedMod calculates tsunami flow speed from the shear velocity required to suspend the quantity and grain size distribution of the observed sand layers. The model assumes a steady, spatially uniform tsunami flow and that sand deposits form from sediment falling out of suspension when the flow stops. Assuming sensitivity analyses test the appropriate parameter values found in nature, flow speeds estimated for the 1700 tsunami range from about 5 to 9 m/s. Using flow depths constrained by tsunami simulations for Cannon Beach, the sediment model calculated flow speeds of 6.5 to 7.6 m/s for sites within ~0.3 km of the beach and higher flow speeds (7.4 to 8.8 m/s) for sites 0.6 to 1.2 km inland. The higher flow speeds calculated for the two sites furthest landward contrast with much lower maximum velocities (<3.8 m/s) predicted by the simulations. Grain size distributions of sand layers from the most distal sites are inconsistent with deposition from sediment falling out of suspension. We infer that rapid deceleration in tsunami flow caused convergences in sediment transport and, therefore, the higher flow speeds calculated by the sediment model may overestimate the actual wave velocity. Key recommendations for future research include investigations focusing on sites with low-relief and simple geography and multidisciplinary studies that couple tsunami sediment models with inundation models to more accurately estimate flow parameters from tsunami deposits.

INTRODUCTION

Sand sheets deposited by a tsunami in the year 1700 CE (Common Era) hold clues to the hydrodynamic properties of waves that inundated coastal lowlands in western Oregon following the most recent magnitude (M_w) 9 Cascadia subduction zone earthquake. Geologic signs of upheaval and flooding preserved in estuaries and coastal lakes that overlie the Cascadia megathrust (Figure 1) chronicle as many as 13 tsunamis triggered by great (M_w >8) earthquakes over the past 4,600 years (Atwater, 1987; Abramson, 1998; Clague et al., 2000; Kelsey et al., 2005). Similar evidence lies beneath wetlands in the lower Ecola Creek valley near Cannon Beach, Oregon (Figure 2), where multiple sandy deposits reveal the widespread extent of the most recent tsunami and its predecessors (Witter 2008). The unprecedented devastation and global impact of the 2004 Indian Ocean tsunami (Lay et al., 2005; Titov et al., 2005) has heightened awareness of the potential for similar giant Cascadia tsunamis along the west coast of North America and motivates further inquiry into the validity of current tsunami hazard maps for vulnerable coastal communities. Yet the sedimentary properties of sand layers, which directly relate to the flow parameters of the wave, have largely been ignored by numerical modeling that provides the underpinnings for tsunami hazard mapping and mitigation.

Many communities located in exposed, low-elevation areas along the Oregon coast face the risk of tsunami inundation. The hazard comes from two principal sources: distant tsunamis that cross the Pacific Ocean produced by earthquakes around the Pacific Rim, and local tsunamis spawned by earthquakes on the Cascadia subduction zone. As of the date of this report, published tsunami inundation maps that predict the severity of ocean flooding cover less than one-third of Oregon's coastal communities that reside in the path of potentially devastating Cascadia tsunamis. In addition, new earthquake source models (Tsunami Pilot Study Working Group, 2006; Priest et al., 2008) developed since the 2004 Indian Ocean tsunami question the accuracy of existing tsunami hazard maps (e.g., Priest et al., 1997a; 1997b; 2002; 2003; Walsh et al., 2000) and suggest that current maps may significantly underestimate potential runup elevations and inland inundation. Extensive sand sheets documented at numerous sites in Oregon, including the lower Ecola Creek valley at Cannon Beach (Figure 2), provide tangible evidence of the impact and extent of prehistoric tsunamis that have invaded the coast. Witter (2008) mapped the extent of Cascadia tsunami deposits at Cannon Beach to evaluate the validity of new earthquake source models and computer simulations for a comprehensive tsunami hazard assessment carried out by Priest et al. (2008).

In this paper we report on the application of an inverse tsunami sedimentation model, TsuSedMod (Jaffe and Gelfenbaum, 2007), that uses the thickness and grain size of the 1700 Cascadia tsunami deposit to predict the peak flow speed of the wave. The purpose of this investigation is to explore the efficacy of this multidisciplinary approach, and evaluate its strengths, weaknesses, and areas of needed improvement. Our work builds on the tsunami deposit mapping of Witter (2008) by determining the physical properties of the 1700 tsunami deposit, including layer thicknesses, trends in grading and grain size distributions. Initial model results suggest that normally-graded sand layers in tsunami deposits located near the beach probably were transported by maximum flow speeds of 6.5 to 7.5 m/s and then settled out of the water column when the flow stopped. Further inland, normally-graded deposits indicate higher flow speeds (>8.5 m/s) relative to sand deposits close to the beach and suggest that spatial

deceleration of flow may have influenced the characteristics of the deposit farther up the valley. Comparisons show that flow speed estimates calculated by TsuSedMod are higher than depth-averaged, maximum flow velocities predicted by tsunami scenarios that have been developed to simulate inundation by a Cascadia tsunami at Cannon Beach.

HISTORY OF TSUNAMI INUNDATION AT CANNON BEACH, OREGON

The small beachside community of Cannon Beach (population 1,640) in northwestern Oregon (Figure 2) faces the risk of flooding by extreme ocean levels from a number of sources, including wind-driven waves during strong eastern Pacific storms, distant tsunamis generated by earthquakes around the Pacific Rim and local tsunamis triggered by rupture of the Cascadia subduction zone. Among these natural hazards, local Cascadia tsunamis pose the greatest risk to the residents and visitors of Cannon Beach and other coastal communities. For instance, geologic evidence testifies that at least three local Cascadia tsunamis in the past 1,000 years have inundated Cannon Beach, flooding more than a kilometer up nearby Ecola Creek valley (Witter, 2008).

The Cascadia subduction zone encompasses the region of deformation that accommodates convergence between Pacific and North American tectonic plates. Within this zone of deformation, the principal source of infrequent, giant (magnitude 9) earthquakes is a ~1000-km-long thrust fault that extends from Cape Mendocino, California to Vancouver Island, British Columbia and projects to the seafloor at the base of the continental slope (Figure 1). Seafloor deformation caused by the most recent magnitude 9 Cascadia earthquake on January 26, 1700 produced a tsunami that damaged villages in Japan (Satake et al., 1996; Satake et al., 2003; Atwater et al., 2005) and left an indelible signature in native American oral traditions (Ludwin et al., 2005). Geologic evidence of drowned wetlands and widespread sand sheets interlayered with sediments beneath estuaries and coastal lakes above the Cascadia megathrust warn of repeated great earthquakes that triggered at least 13 tsunamis over the last 4,600 years (Atwater and Hemphill-Haley, 1997; Clague et al., 2000; Witter et al., 2003; Kelsey et al., 2005). Careful study of offshore turbidites suggests a longer record spanning the Holocene of 20 undersea landslides triggered by Cascadia earthquakes capable of generating large tsunamis on average every 500 years (Goldfinger et al., 2003).

More recently, onrushing seawater flooded Cannon Beach in March 1964 when a distant tsunami produced by the magnitude (M_w) 9.2 Prince William Sound earthquake in southeastern Alaska reached the coast of Oregon. The event demonstrated that coasts of the western United States face hazards from distant tsunamis in addition to local Cascadia tsunamis. The 1964 Alaska tsunami, with the highest impact among the 20 distant tsunamis reported along the Oregon coast since 1854, killed 4 people near Newport, one person in Seaside, and caused over $920,000 in damages across the state (Lander et al., 1993; Dunbar and Weaver, 2007).

IMPACT OF THE 1964 ALASKA TSUNAMI AT CANNON BEACH, OREGON

Shortly after 11:34 pm local time on Friday, March 27, 1964 a tsunami inundated Cannon Beach (Lander et al., 1993) during a rising tide (*The Sunday Oregonian,* March 29, 1964, p. 40), after

traveling approximately four hours from its Alaskan source, the magnitude (M_w) 9.2 Prince William Sound earthquake. An eyewitness report of the tsunami impacts at Seaside, 13 km to the north, noted that the ocean withdrew to an elevation of -0.6 m below mean lower low water (MLLW) before the first surge arrived, which reached runup elevations of 6.7 to 7.9 m (MLLW) along the ocean front (Horning, 2006).

Wave runup at the ocean front in Cannon Beach probably did not exceed 6.1 m (MLLW) because there are no reports or other evidence to suggest the tsunami overtopped the 6.1- to 7.0-m-high (MLLW) foredune ridge that fronts the beach. Newspaper reports of water depths at two sites suggest maximum water elevations in Cannon Beach reached 5.8 to 6.1 m (MLLW). A second surge reached lower elevations at Cannon Beach at around 3:30 am local time causing little or no damage (*The Sunday Oregonian,* March 29, 1964, p. 40).

Photographs (Figure 3) illustrate the tsunami's impact at Cannon Beach where waves damaged city infrastructure at a cost of $50,000 and caused $180,000 in losses to private property based on estimates from the Oregon State Civil Defense Agency in April of 1964 (Spaeth and Berkman, 1967). The tsunami broke a ~60-m-long primary bridge across Elk Creek, now named Ecola Creek, into two sections and carried both approximately 275 m upstream to a low-lying meadow on the northeast bank of the creek. A 4.9-m-long drift log borne by strong currents crashed through a window of the Bell Harbor Motel (*Seaside Signal*, April 2, 1964, p. 1) causing extensive water damage and strewing debris (Figures 3b and 3c). The force of the wave also tore one unit of the Buoys and Gulls Motel from its foundation, transporting the house approximately 460 m inland (*Seaside Signal,* April 2, 1964, p. 7) to rest between the two bridge sections (Figure 3d).

Witter (2008) reconstructed the total extent of inundation by the 1964 Alaska tsunami from eyewitness observations of water depth and by interpolation using a digital topography with 2-foot contours provided by the city (Figure 4). Eyewitnesses contend that water depths reached 5-ft (1.5-m) deep at the Bell Harbor Motel (*The Sunday Oregonian,* March 29, 1964, p. 40), 2.5-ft (0.8-m) deep at a house owned by William and Sally Steidel and as much as 1 ft (0.3 m) of water remained on the City's main street after the initial wave (*Seaside Signal*, April 2, 1964, p. 1). Schlicker et al. (1972) reported flooding of two City blocks in downtown Cannon Beach. Based on reports of damage to the Highway 101 bridge across Ecola Creek (Spaeth and Berkman, 1967), the tsunami flooded at least as far inland (east) as the highway embankment (Figure 4). However, no reports indicated that waves overtopped the highway.

COMPARISON TO RESULTS OF THE ALASKA 1964 TSUNAMI SIMULATION

A numerical simulation of the 1964 tsunami at Cannon Beach by Priest et al. (2008) closely matched the extent of inundation estimated from historical accounts by Witter (2008) (Figure 4). The simulation predicted flow depths of 1.6 m at the Bell Harbor Motel and 0.8 m at the Steidel House. The simulation also closely matched shallow water depths (~0.3 m) reported in downtown Cannon Beach. At the foredune that fronts Cannon Beach, 1964 tsunami runup reached an estimated elevation of 6.1 m (NAVD88); the simulation predicted 6.7 m. Simulated inundation on the landward side of the foredune is slightly less than that estimated from historical accounts (Figure 4), but the historical inundation is highly uncertain in this area. For

instance, one eyewitness recounted that water from the tsunami flooded the city from the east as waves inundated the creek and surrounding wetlands leaving parts of the area dry, including the main water pump station at 2nd and Spruce Streets and the dikes surrounding two waste water lagoons (Les Wierson, personal communication, 2008). Alterations to the landscape, including the construction of artificial levees for flood control, have changed the area since 1964. Priest et al. (2008) reasoned that uncertainties in geometry of the Prince William Sound earthquake source, nonlinear tidal effects, and the small (~0.3 m) difference between the tide used in the simulation and the actual tide on March 27, 1964, may account for some of the differences between the observed and simulated tsunami inundation.

APPROACH AND METHODS

We developed a multidisciplinary approach that combines aspects of sediment transport modeling (Jaffe and Gelfenbaum, 2007), stratigraphic analyses (Witter, 2008; Peterson et al., 2008; Gallaway et al., 1992) and numerical tsunami simulations (Priest et al., 2008) to place better constraints on the hydrodynamic flow parameters of the 1700 tsunami at Cannon Beach, Oregon. Our principal objective is the application of a simple sediment transport model (Jaffe and Gelfenbaum, 2007) that uses the physical characteristics of tsunami deposits, including layer thickness and particle size characteristics, to predict maximum flow speed (Figure 5). Here we apply the model using the physical properties of sand layers deposited by the 1700 tsunami at Cannon Beach. Finally, we compare the results of tsunami sediment modeling to maximum flow velocities predicted by numerical tsunami simulations completed for a comprehensive tsunami hazard assessment at Cannon Beach (Priest et al., 2008).

Grain size distributions for each deposit were determined by standard methods at the U.S. Geological Survey's Coastal and Marine Geology sedimentology laboratory in Menlo Park, California. All sediment samples were dried and weighed prior to treatment with 10 mL of 35% hydrogen peroxide to oxidize organic matter. Hydrogen peroxide was evaporated by heating. Once cool, samples were placed in a centrifuge for 30 minutes at 1500-1700 rpm to remove soluble salts. An A.S.T.M. #230 sieve was used to separate each sample into sand and fines size fractions (no samples contained gravel). To each cylinder containing the fine fraction we added 5 mL of 10% sodiumhexametaphosphate (Calgon) to disperse clay particles. 20 mL aliquots of the fine fractions were drawn by pipette, allowed to dry and weighed. We used a Beckman Coulter Laser Sizer Particle Analyzer (LS100) to calculate settling velocity of the fine fractions following the method of Dietrich (1982) and using a particle density of 2.65 g/cm^3. After drying and weighing the sand fractions, we characterized sand particles from their settling velocities using 2-m-long Rapid Settling Assessment (RSA) settling tubes. The total grain size distributions for each sample were determined by combining the sand and fines particle analyses using pcSDSZ version 1.23 computer software. Grain size measurements were determined at ¼-phi intervals because grain size strongly influences estimates of tsunami flow speed.

Although this report primarily focuses on sediment transport modeling, the results of a companion study by Witter (2008) provide the framework from which we interpret the origin and extent of sand sheets deposited by prehistoric Cascadia tsunamis in the lower Ecola Creek valley.

The approach used to map tsunami deposits is summarized below. Refer to Witter (2008) for a more detailed description of methods.

Witter (2008) mapped the extent of sand sheets preserved in the subsurface stratigraphy beneath the lower Ecola Creek valley and evaluated their origins whether by tsunami or flooding of Ecola Creek. Using a 2.5-cm-diameter gouge core, Witter investigated one hundred and seventy-seven sites to determine the presence or absence of sand layers that interrupt sequences of freshwater peat and mud underlying the floodplain and wetlands of Ecola Creek (Figure 2). Dense vegetation or cover material obscured almost all natural outcrops along the active creek channel and high ground water obviated shallow shovel pits. We used a Trimble 5700/5800 Real-Time Kinematic Differential Global Positioning System (GPS) to measure the vertical positions (NAVD 88) of core sites sampled for this study. The elevations of less accessible sites or sites with standing water were estimated by interpolation or by surveying the elevation of the contiguous water surface.

Witter (2008) considered ten criteria that support a tsunami origin to assess whether a sand layer was deposited by a prehistoric tsunami or some other process (Table 1). The criteria rely on key sedimentary characteristics of sandy deposits that distinguish tsunami-lain sand from sediment deposited by river floods or storm surges (Peters et al., 2007). For instance, evidence of landward-directed flow, distinctive sand composition and texture, geochemical indicators and the presence of marine or brackish diatoms have all been used to infer a marine rather than a river source for sandy deposits (e.g., Atwater, 1987; Darienzo and Peterson, 1990; Hemphill-Haley, 1995; Atwater and Hemphill-Haley, 1997; Benson et al., 1997). Tsunami deposits have been distinguished from storm-related deposits on the basis of their spatial extent. Tsunamis often deposit sand over many hectares whereas overwash fans produced by storm waves that overtop sand spits usually cover less than a hectare. Sedimentary structures also offer clues that can discriminate thick (tens of cm) normally graded beds of sand deposited out of suspension by a tsunami from thinner, cross-laminated storm deposits with bedform structures that reflect entrainment processes (Tuttle et al., 2004; Nelson and Leclair, 2006). Often, linking a sand layer to stratigraphic evidence of vertical deformation caused by an earthquake provides the strongest case for a tsunami origin (Atwater, 1987).

Conifer needles, moss, herbaceous seeds and other identifiable plant remains entombed in sand deposits were submitted to Beta Analytic Inc. for radiocarbon dating using the accelerator mass spectrometry (AMS) technique. The plant fossils were removed from samples of sand using a 0 phi (1-mm) wet sieve, cleaned of all sediment and young rootlets, rinsed with tap water and air dried. Because the sample material is detrital and likely died before being incorporated in the sand deposit, lab-reported conventional radiocarbon ages, calibrated using the computer program Calib Rev 5.0.1 (Stuiver and Reimer, 1993) and the IntCal04 calibration dataset of Reimer et al. (2004), provide maximum-limiting estimates of the time of sand deposition (Table 2).

Table 1 Summary of evidence for sand layers deposited in the lower Ecola Creek valley that satisfy criteria for a Cascadia tsunami origin.

Sand layer	Deposit has attributes of beach sand*	Presence of modern brackish-marine diatoms	Deposit thins/grain size fines landward	Normally-graded beds observed	Ripup clasts present in deposit	Sharp or eroded lower contact	Organic debris present at top of deposit	Extent of deposit (km)[§]	Deposit is coincident with earthquake-subsided soil	Age overlaps with evidence for regional Cascadia event[#]
1	✓	no	✓	✓	✓	✓	✓	1.45	✓	✓
2	✓	✓	✓	✓	✓	✓	✓	1.40	no	✓
3	✓	✓	✓	✓	✓	✓	✓	1.60	**I**	✓
4	no	**I**[†]	no	no	no	✓	✓	2.20	no	✓

Note: check (✓) indicates the evidence was observed at multiple sites; **I**, data are insufficient to provide conclusive evidence; "no" indicates the absence of evidence.

*Beach sand component interpreted from sand mineralogy and grain size (see Table 2 in Witter, 2008).

[†]Rare fossil marine diatoms identified in sand layer 4 were also present in silty sediment above and below the sand layer. Sand sheet distribution shown in Figure 6 and other physical attributes of sand layer 4 suggest a river source and that fossil marine diatoms were likely reworked from Tertiary Astoria Formation marine mudstone present in the upper watershed of Ecola Creek.

[§]Landward extent of deposit measured from mouth of Ecola Creek to core site furthest inland where sand sheet was observed. Only tsunamis or high-stream flow could explain such widespread deposits in the lower valley, ruling out storm waves superimposed on extreme ocean levels as an alternative explanation.

[#]Correlations based on regional geologic records of Cascadia earthquakes and tsunamis shown on Figure 7.

SUMMARY OF EVIDENCE FOR PREHISTORIC CASCADIA TSUNAMIS

Interbedded within organic-rich, fresh-brackish sediments beneath the lower Ecola Creek floodplain and surrounding wetland, four sand sheets have been correlated in gouge cores that extend 1-to-2-km up the valley (Figure 6). Several processes are capable of depositing sand layers in this environment, including high creek flows during winter floods, ocean storms coincident with high tides and tsunamis generated by distant sources and local Cascadia earthquakes. Witter (2008) demonstrated that three of the most extensive sand sheets exhibit evidence of a beach source, transport by marine water and satisfy multiple criteria that support a Cascadia tsunami origin (Table 1). A few very thin and discontinuous sand layers are best explained by extreme floods of Ecola Creek or possibly inundation by the 1964 Alaska tsunami.

The three youngest, widespread sand deposits (sand layers 1, 2 and 3) mapped beneath the lower Ecola Creek valley (Figures 7 and 8) meet 9 out of 10 criteria that support a case for a Cascadia tsunami as the emplacement mechanism (Table 1). Because each deposit exhibits evidence of a beach or marine origin, Witter (2008) ruled out flooding of Ecola Creek as an alternative explanation. For example, all three sand layers possess similar characteristics of the modern beach and dune sand west of Cannon Beach, including an abundance of well-sorted, fine-textured quartz and rounded augite grains. In addition, two of the deposits (sands 2 and 3) contain elevated numbers of brackish-marine diatoms, including, *Fragilaria schulzii*, a diagnostic species that lives on sand grains in nearshore marine environments (Krammer and

Table 2 Calibrated age estimates of sand sheets in the lower Ecola Creek Valley derived from AMS radiocarbon dates on detrital macrofossils.

Sand layer no.*	^{14}C lab number[#]	Core Number[†]	Sample depth in core (m)	Material dated	$\delta^{13}C$ (‰)	Lab-reported age (^{14}C yr BP at 1σ)[§]	Calibrated age (cal yr BP at 2σ)**	Relative area under probability distribution[##]	Preferred age estimate for sand layer[††]
1	228613	POMP-1	0.46	needles, moss, seeds	-27.2	90 ± 40	12-148	0.69	**144-270**[§§]
							187-199	0.02	
							211-269	0.27	
2	219693	CANB-69	0.96	moss	-28.0	570 ± 40	521-570	0.40	**520-800*** **
							580-651	0.60	
	230216	CANB-43R	1.25	needles, moss, seeds, twig	-27.3	790 ± 50	658-795	0.99	
3	220572	CANB-W	0.62	conifer needles	n.d.	990 ± 60	765-1004	0.97	**910-980**[###]
							1030-1052	0.03	
	230217	CANB-43R	1.39	needles, moss, seeds, twig	-30.0	1000 ± 50	788-989	0.97	
							1031-1051	0.03	
	219694	CANB-69	1.04	moss	-24.3	1050 ± 40	916-1058	1	
4	220573	CANB-62	1.35	conifer cone	-24.5	1430 ± 50	1276-1411	1	**1280-1410**

*Radiocarbon age data grouped by sand sheet number determined by stratigraphic correlation. Sand sheet numbers increase with age.
[#]All samples submitted to Beta Analytic , Inc., Miami, Florida for ^{14}C dating using AMS techniques.
[†]Core number designates locality and specific core identified by letter. The localities are abbreviated as follows: CANB, Cannon Beach.
[§]Conventional ages reported by radiocarbon laboratory based on the Libby half life (5570) for ^{14}C.
**Calibrated age ranges before AD 1950 reported to the nearest year using the computer program Calib Rev 5.0.1 (Stuiver and Reimer, 1993) and the IntCal04 calibration dataset of Reimer et al. (2004) with a lab error multiplier of 1.0 and reported to 2σ.
[##]Age intervals with less than 0.01 relative area under the distribution not shown.
[††]Age ranges rounded to the nearest decade except for historical constraints on the estimate for sand layer 1.
[§§]Upper bound of age range constrained by the year 1806 when Lewis and Clark reached Ecola Creek and written history began in coastal Oregon.
*** Age range represents the sum of probabilities for both ^{14}C ages for sand layer 2. The two samples meet a Xi-square test that shows a statistical difference at the 95% level.
[###] Age range represents 97% of the relative area of the calibrated age distribution for the pooled mean age of the three ^{14}C dates for sand layer 3. The three ages are indistinguishable based on a Xi-square test for statistical difference at the 95% level.

Lange-Bertalot, 1991; Witkowski et al., 2000). Witter (2008) also found evidence that the deposits became thinner (Figure 6) and texturally finer further inland, supporting a marine source and not high stream flow of Ecola Creek. Other attributes of the sand sheets, noted as distinctive features in historic tsunami deposits worldwide (Peters et al., 2007), include normally-graded beds, muddy ripup clasts, sharp or eroded lower contacts and organic debris capping each deposit (Table 1). Witter (2008) precluded winter storms as an alternative explanation because all three deposits extend 1.4 to 1.6 km inland (Figure 6), far beyond the reach of storm waves superimposed on extreme ocean levels historically (Witter et al., 2001). Further support for a tsunami origin for all three sand layers comes from age estimates that overlap times reported for great earthquakes and tsunamis at other sites above the Cascadia subduction zone (Figure 9).

In contrast to the youngest three sand deposits, sand layer 4 satisfies far fewer criteria consistent with a tsunami origin (Table 1). Witter (2008) showed that sand 4 lacks the attributes of beach sand, and instead contains abundant rock fragments and angular pyroxene grains characteristic of sand in the modern creek channel. The widespread extent of sand 4 and its similar age to evidence elsewhere for a Cascadia earthquake and tsunami about 1250 years ago suggest that sand 4 might be a tsunami deposit (Figure 9). However, despite field mapping by Witter (2008) and Peterson et al. (2008) that tracked the deposit for over 2.2 km up the valley, the furthest extent of all the sand layers identified, neither the extensive coverage of the deposit nor its age rules out a creek flood as an alternative explanation. Witter (2008) also noted a distinct absence of evidence for earthquake related subsidence associated with the sand deposit. Its apparent chaotic distribution along the central axis of the valley (Figure 6), the absence of a landward-thinning deposit, no observed ripup clasts and generally massive nature argue against emplacement by tsunami. During field reconnaissance, we observed deposits similar to sand 4 that mantled the creek's levee after a series of winter storms in February 2007. Witter (2008) concluded that sand 4 most likely reflects flooding of Ecola Creek based on its distribution along the central axis of the valley (Figure 6) and its massive texture and mineralogy that resembles sandy flood deposits within the natural creek levee.

Rare and discontinuous sandy lamina, often no thicker than several fine sand grains and at different stratigraphic depths, were noted in many core descriptions of Witter (2008). Field examination identified a mix of quartz and lithic grains in the lamina, suggesting a combination of beach and creek sources. Several explanations can account for these thin sands interlayered with peaty deposits beneath wetlands along Ecola Creek. Sand thrown aloft by strong westerly winds during winter storms could mantle marshes with thin, discontinuous layers of fine aeolian sand. Bioturbation and liquefaction (Peterson et al., 2008) have been proposed as other reasonable explanations. However, one of two processes probably explains best the youngest sand lamina observed at several sites in Pompey Marsh: the 1964 Alaska tsunami or the 1967 flood. In their summary of the effects of the 1964 tsunami at Cannon Beach, Lander et al. (1993) write, "The water poured down the street carrying logs, debris and sand everywhere between the buildings and littering the street." Witter (2008) postulated that the tsunami also left a layer of sand and debris in the wetlands adjacent to the City. Alternatively, the 1967 flood also may have left a visible layer of sand in the geologic record considering historical accounts of at least 2.5 ft (0.8 m) of water in downtown Cannon Beach (O'Donnell, 1996). Too few traces of the youngest sand lamina and its discontinuous distribution prevent a thorough evaluation of criteria that favor a tsunami over a flood origin.

MICROFOSSIL EVIDENCE FOR COSEISMIC LAND-LEVEL CHANGE IN 1700

Preliminary analyses of fossil diatoms from sediment above, within and below the 1700 tsunami deposit suggest the wave was preceded by a sudden vertical drop in land level caused by a regional Cascadia earthquake. Assemblages of fossil diatoms counted in peat below the 1700 sand layer includes an assortment of benthic species found in both freshwater and high marsh environments (Figure 10). Species identified within the tsunami deposit represent a mixture of both benthic and planktonic diatoms from freshwater, brackish and marine environments. The presence of *Thalassiosira* spp., a planktonic marine diatom, strengthens the case for sand deposition by tsunami. Further evidence that favors a tsunami origin for the sand is the obvious change in the assemblage of fossil diatoms examined in the peaty mud overlying the sand (Figure 10). An abundance of diatoms found in high to low tidal marsh environments indicates a sudden drop from predominantly freshwater conditions evident by diatoms in peat that underlie the 1700 sand sheet. We infer that this shift in diatom assemblages reflects rapid subsidence of the coast during the great earthquake that generated the 1700 Cascadia tsunami. Because we lack modern analogs for the fossil assemblages found at Cannon Beach, we cannot precisely estimate the amount of subsidence that accompanied the earthquake.

STRATIGRAPHY AND SEDIMENTOLOGY OF THE 1700 TSUNAMI DEPOSIT

The 1700 tsunami deposit is thickest (>0.1 m) at Pompey Marsh near the mouth of Ecola Creek (Figures 6 and 7) and thins inland over more than 1.4 km as revealed in sediment cores along the southeastern margin of the valley (Figure 8). Distinctive black peat underlies the sand layer across a clear (3 to 10 mm) to sharp (≤3 mm) contact aiding in correlation between sites (Figure 7 and 11). Field observations noted by Witter (2008) indicate that the sand is well-sorted, fine-grained and consists of abundant quartz grains (Figure 11a). In many cases the uppermost part of the deposit consisted of a mix of sand and detrital organic debris (Figure 11d). Heavy mineral analyses of the sand determined that rounded augite grains, abundant in beach sand, outnumbered angular grains more common in creek channel sand, implying a beach source for the deposit (Peterson et al., 2008). In some cores, clasts of peat or inorganic mud mixed in the deposit suggest that erosive currents placed the sand (Figure 11b).

We sampled the 1700 tsunami sand sheet in sediment cores at 6 sites (Table 3), extending from core C located 300 m from the beach (Figure 11a) to core X located 1.2 km to the southeast and up the valley (Figure 2). The sand deposit varied in thickness from 9 cm in core C to 1.5 cm in core 45. In three of the six cores examined the sand deposit consisted of 2 or 3 normally graded sandy interbeds (Figures 11a and 11c). We subsampled each deposit at 0.5- to 1-cm-thick intervals guided by field observations of grain size trends and contacts between sand beds. Appendix A includes the complete grain-size results from laboratory analyses. Fine sand dominates all samples as illustrated by grain size distributions that peaked between 2.25 to 2.75 phi (149 to 210 μm) (Figure 12). Mean grain sizes of the sand samples indicate that the 1700 tsunami deposited predominantly fine sand close to the beach with an increasing component of silt (up to 20 to 30%) further inland. The coarsest samples occurred at core sites C, 8 and 11 (Table 3) with mean grain sizes that varied between 2.5 to 3.0 phi (125 to 177 μm). Increasing silt and clay intermixed with sand further inland raised the means to 2.75 to 5 phi (31 to 149 μm) for samples from cores 14, 45 and X (Table 3) Mean grain sizes of all samples were

Table 3 Grain size characteristics and statistics for samples of sand deposited by the 1700 Cascadia tsunami in Cannon Beach, Oregon.

Core No.*	Sand Bed Interval (cm)	Sample Interval (cm)	% Sand	% Silt	% Clay	Mean Phi	Skewness	Kurtosis	Field Description
C [300]	33-35	33-34	95.34	3.25	1.41	2.58	4.91	28.14	Field examination inferred three fining upward sand beds. Field description of 33-35: grey, fine-grained, quartz-rich sand.
		34-35	97.07	2.16	0.77	2.57	4.89	38.55	
	35-37.5	35-36.5	98.01	1.43	0.56	2.41	7.44	64.18	Field description of 35-37.5: clean, white to grey, fine quartz-rich sand with large black peat clast on lower contact.
		36.5-37	98.28	1.28	0.44	2.50	7.79	73.63	
	37.5-42	38-39	92.94	5.74	1.32	2.64	4.09	20.87	Field description of 37.5-42.5: grey, fine-grained, quartz-rich sand with abundant detrital debris, including conifer (spruce) needles (see Figure W).
		39-40	95.85	2.82	1.32	2.63	5.14	30.72	
		40-41	**95.20**	**3.83**	**0.97**	**2.67**	**5.18**	**32.63**	
		41-42	**96.28**	**3.03**	**0.69**	**2.51**	**5.72**	**39.44**	
8 [305]	38.5-41.5	38.5-39.5	96.52	2.48	1.00	2.59	5.66	37.39	Only a single bed was discerned in the field (see Figure X). Field examination of the sand noted woody debris and peat rip-up clasts within deposit.
		39.5-40.5	96.81	2.27	0.92	2.48	6.08	43.21	
		40.5-41	**98.10**	**1.30**	**0.60**	**2.50**	**7.76**	**70.89**	
		41-41.5	**97.91**	**1.54**	**0.54**	**2.45**	**7.68**	**69.86**	
11 [315]	37-39	37-38	86.72	10.27	3.01	2.91	2.89	11.04	Two sand beds discerned from field examination (see Figure Y). Field description: fine quartz-rich sand mixed with peat.
		38-38.5	**82.59**	**12.28**	**5.14**	**2.78**	**4.04**	**19.79**	
		38.5-39	**67.42**	**23.57**	**9.01**	**2.50**	**6.03**	**42.93**	
	39-40.5	39-40	76.88	15.91	7.21	2.64	5.20	33.59	Field description: fine quartz-rich sand mixed with peat.
		40-40.5	68.98	21.93	9.09	3.15	2.17	7.50	
14 [600]	61.5-64	60-61†	94.73	3.90	1.37	2.72	4.66	26.03	Field observations note a single sand bed from 61.5-64 described as grey, fine-to-medium grained, quartz-rich sand (see Figure Z). A layer of detrital debris overlies the sand bed from 54-61.5.
		61-62†	91.70	6.24	2.06	2.82	3.55	15.73	
		62-63	**90.47**	**7.77**	**1.76**	**2.87**	**3.38**	**15.04**	
		63-63.5	**82.26**	**14.40**	**3.34**	**3.14**	**2.25**	**7.39**	
		63.5-64	78.28	18.08	3.64	3.31	1.96	6.01	
45 [860]	53-57.5	53-54.5	47.17	36.92	15.90	4.99	0.48	1.87	Examination of sediment core noted two apparent beds of sand mixed with peat. Sand bed from 53-57.5 described as patchy, fine-grained sand mixed in peat that fines upward.
		54.5-55.5	55.87	30.80	13.33	4.49	0.72	2.09	
		55.5-56.5#	n.d.	n.d.	n.d.	n.d.	n.d.	n.d.	
		56.5-57.5	68.98	21.93	9.09	3.80	1.27	3.32	
	57.5-62	57.5-59	76.88	15.91	7.21	3.63	1.73	4.83	The lower sand bed from 57.5-62 was patchy, fine-grained sand mixed in peat that fined upward.
		59-60	**67.42**	**23.57**	**9.01**	**3.88**	**1.29**	**3.42**	
		60-61	**82.59**	**12.28**	**5.14**	**3.16**	**2.18**	**6.74**	
		61-62	74.30	18.40	7.30	3.67	1.59	4.39	

Table 3 (Continued.)

Core No.	Sand Bed Interval (cm)	Sample Interval (cm)	% Sand	% Silt	% Clay	Mean Phi	Skewness	Kurtosis	Field Description
X [1225]	50-52	**50-51**	**73.23**	**19.18**	**7.59**	**3.65**	**1.55**	**4.12**	A single sand bed was observed in the field and described as muddy, fine-grained sand.
		51-52	**74.30**	**18.12**	**7.58**	**3.53**	**1.59**	**4.20**	

Note: Figures in bold show data for samples used as inputs for sediment transport modeling.
*Values in brackets represent distance in meters from core site to the beach.
†Sample includes detrital organic material from overlying debris layer.
#Sample interval 55.5-56.5 was spilled in lab and lost during sample preparation.

always finer than beach sand, which has a mean of 2.25 phi (210 μm) based on an analysis by Witter (2008). Comparison of sample means in many cases confirmed evidence of normal (fining-upward) grading observed for individual sand beds examined in the field. However, some samples showed reverse grading with distinct coarsening-upward trends near the base of the deposit (e.g., core 11, 39-40.5 cm, Table 3).

RESULTS OF SEDIMENT TRANSPORT MODELING

EVIDENCE FOR SAND SETTLING FROM SUSPENSION

The tsunami sedimentation model of Jaffe and Gelfenbaum (2007) operates under the simple assumption that the thickness and grain size distribution of specific intervals of the deposit form from sand particles settling out of suspension. Among the six examples of the 1700 tsunami sand examined for this study, particular layers of the deposit showed both normal (fining upward) grading and reverse (coarsening upward) grading. For model inputs, we selected consecutive layers from each core that showed evidence for normal grading based on changes in the mean phi value. Model results for four of the six examples reproduce the observed normal grading (Figure 12), which implies that particular layers of the 1700 tsunami deposited out of suspension. Grain size distributions best fit by the model included the samples from core sites nearest the beach (cores C, 8, 11 and 14). Although samples from cores further inland (e.g., cores 45 and X) also showed evidence for normal grading, the sand particle distributions calculated by the model showed poorer matches (Figure 12) and suggest deposition by another process or a combination of mechanisms.

TESTS OF MODEL PARAMETER SENSITIVITY

We explore the sensitivity of average tsunami flow speeds calculated by the model by varying specific parameters, including bed roughness, the resuspension coefficient and tsunami flow depth, all poorly constrained model inputs that are difficult to estimate for paleotsunami deposits. Another model parameter, the eddy viscosity profile, determines the vertical variation in turbulent stress for overland flow during tsunami inundation. We did not examine the model sensitivity to this parameter here. However, tests using three different eddy viscosity profile shapes by Jaffe and Gelfenbaum (2007) showed that average tsunami flow speeds calculated by TsuSedMod are relatively insensitive to vertical variations of turbulent stress. Our calculations use the eddy viscosity profile developed by Gelfenbaum and Smith (1986) that fits laboratory data for steady uniform flow. We test the effect of two additional input parameters, grain size and deposit thickness, on model calculations presented below in the section on Flow Speed Calculations. Initial tests varying these inputs show that sediment grain size strongly influences calculated tsunami flow speeds, but model results are less sensitive to the deposit thickness (Jaffe and Gelfenbaum, 2007). Considering the model's sensitivity to the parameters tested, and assuming the parameter ranges span the natural variability in the tsunami process, we compute maximum flow speed estimates of about 5 to over 9 m/s for the 1700 tsunami.

Bed Roughness

Average tsunami flow speed decreases with increasing bed roughness. The model calculates bed roughness from combined grain and sediment transport roughness according to the formulation of Wieberg and Rubin (1989). Testing the model's sensitivity to this parameter, we varied bed roughness by an order of magnitude while holding water depth constant at 5 m and using grain sizes and deposit thicknesses for sand layers sampled at three sites (Figure 13). Varying bed roughness by an order of magnitude produced a 28 to 30% change in calculated flow speed. Varying bed roughness at smaller values produced a greater percent change in flow speed than varying the parameter at higher values. For instance, changing bed roughness from 2.5×10^{-5} to 5.0×10^{-5} produced a 9% decrease in average flow speed. Whereas, changing bed roughness from 22×10^{-5} to 26×10^{-5} only produced a 2.5% decrease in flow speed.

We also ran tests on the effect of varying bed roughness on flow speed using different flow depths (Figure 14). Since the model is somewhat sensitive to bed roughness, additional test runs varied water depth from 1 to 5 m to explore a larger range of flow speed estimates. Generally, decreasing the flow depth input parameter results in higher calculated flow speeds. We discuss estimates of water depth and their effect on model outputs more completely below. Flow speeds calculated for two sites, cores C and 8, using a variety of water depths and bed roughness values ranged from 4.7 to 9.3 m/s.

Resuspension Coefficient

TsuSedMod calculates the amount of sediment suspended in the water column as a function of the resuspension coefficient (Jaffe and Gelfenbaum, 2007). One of the least constrained and most influential parameters of the model, resuspension coefficients in nature have been reported to vary from 10^{-5} to 10^{-3} in estuary and continental shelf settings (Drake and Cacchione, 1989; Vincent et al., 1991). Using a constant water depth of 5 m, we varied the resuspension coefficient between 1.4×10^{-5} and 1.4×10^{-3} to study its effect on flow speed (Figure 15). The tests run for this study show similar results to sensitivity tests performed by Jaffe and Gelfenbaum (2007). An order of magnitude increase in the resuspension coefficient from 1.4×10^{-5} to 1.4×10^{-4} requires a 33 to 35% lower flow speed to match the properties of the sand deposit. Decreasing the coefficient by an order of magnitude, from 1.4×10^{-5} to 1.4×10^{-4}, results in a 74 to 80% increase in the calculated flow speed. Changing the resuspension coefficient for smaller values has greater influence on flow speed because the concentration of suspended sediment decreases exponentially with elevation above the bed (Jaffe and Gelfenbaum, 2007). As a result, higher flow speeds are required to suspend the same amount of sediment when the model uses a lower resuspension coefficient. The range of flow speeds calculated for this test using inputs for four sand layers varied from 4.4 to 14.4 m/s.

Tsunami Flow Depth

Flow speed calculated by TsuSedMod is relatively insensitive to high flow depths and becomes increasingly sensitive to decreasing flow depths below about 2 m (Figure 16). Similar to the effect of changing the resuspension coefficient, higher flow depths have less influence on the calculated flow speed because the concentration of sediment suspended in the water column decreases exponentially with height above the bed. For example, doubling the flow depth from 5 to 10 m has relatively little effect, resulting in a 3 to 6% decrease in flow speed. However,

decreasing the flow depth from 2 to 1 m requires a 9 to 11% increase in flow speed to suspend the amount of sediment in the tsunami deposits we examined.

Independent constraints on tsunami flow depth can be derived from field evidence, tsunami inundation modeling, or from the relationship between flow depth and wave speed, known as the Froude number. Detailed surveys measuring water marks on buildings, broken branches, the elevation of debris left in trees and other evidence provide estimates of the minimum flow depths reached by recent historical tsunamis (Bourgeois et al., 1999; Kawata, 1999; Gelfenbaum and Jaffe, 2003; Borrero, 2005). Although flow depths of prehistoric tsunamis are more difficult to estimate, some workers have attempted to reconstruct minimum runup elevations from the distribution of sand deposits behind coastal dunes or barrier spits (Peterson et al., 2007). In this study, model estimates of the 1700 tsunami flow speed used a range of flow depths specified by selected numerical tsunami simulations for Cannon Beach (Priest et al., 2008). The rationale for using the simulations as well as Froude numbers as constraints on flow depth is presented in the Discussion section.

FLOW SPEED CALCULATIONS

We apply the tsunami sediment transport model, TsuSedMod (Jaffe and Gelfenbaum, 2007), to estimate the average flow speed of the 1700 tsunami using laboratory measurements of the grain size distribution and thickness of sand layers deposited by the wave (Figure 17). The model calculation involves multiple iterations that vary the shear velocity until the sediment source distribution determined by the model matches the properties of the observed deposit. A flow speed profile is calculated as follows:

$$U(z) = \int_{z_0 total}^{z} \frac{U_*^2}{K(z)} dz$$ (Equation 12 of Jaffe and Gelfenbaum, 2007)

where U^* is shear velocity, z is the elevation above the bed, $z_{o_{total}}$ is the combined grain and sediment transport bed roughness, and $K(z)$ is the eddy viscosity. Depth averaged flow speed is obtained by dividing the integral of the flow speed profile by the flow depth. Sensitivity tests show that the calculated flow speed is strongly influenced by grain size but less dependent on deposit thickness (Jaffe and Gelfenbaum, 2007).

We selected Cannon Beach as a study area to apply TsuSedMod because of the presence of an extensive sand sheet deposited by the 1700 tsunami, the relatively simple geometry of the lower Ecola Creek valley, its low topographic relief and gradient, and to expand on a comprehensive tsunami hazard assessment (Priest et al., 2008; Witter, 2008). Inputs for the modeling come from measurements of the sedimentary characteristics of sand deposited by the 1700 tsunami at six sites (Figure 2). Model inputs include grain size distributions, thicknesses of sand layers displaying normal grading, and estimated maximum flow depth. These inputs and the modeling results are shown in Figure 17.

Peak tsunami flow depths for each core site were specified by tsunami simulations for Cannon Beach that account for changes in topography related to the emplacement of artificial fill and coastal erosion (Figure 18) (see Priest et al., 2008). The approach used to modify the digital elevation model (DEM) that serves as the grid foundation is summarized below. The simulations use the SELFE inundation model described by Zhang and Baptista (2008). Model inputs

represent average flow depth rounded to the nearest meter for two simulations, Average 9 (run 268) and Average 14 (run 259). We do not know if the tsunami scenarios accurately reflect the actual flow depths of the 1700 tsunami. Therefore, because of the large uncertainties in simulating the 1700 tsunami, flow depths plotted on Figure 17 include an error of ± 1 m. If the maximum flow depths from tsunami simulations overestimate the actual 1700 tsunami flow depths, then the sediment transport model calculations underestimate the actual flow speeds.

Flow speeds calculated by TsuSedMod using inputs for grain size and deposit thickness for six samples of the 1700 tsunami deposit are plotted in Figure 17. Error bars represent the range of calculated flow speeds based on a 1 m uncertainty in flow depth for each sample location. The estimated flow speeds range from 6.5 to 7.6 at sites in Pompey Marsh about 300 m from the beach and increase to 8.8 m/s at core X, 1200 m inland. The trend in these data show an unexpected increase in velocity inland (Figure 17). Further modeling is necessary to evaluate whether this increase in flow speed reflects the actual variation in tsunami velocity or poor model performance due to a convergence in sediment transport, or a combination of factors.

We compared tsunami flow speed calculated by the sediment transport model to flow velocities predicted by three different tsunami scenarios completed for the Cannon Beach tsunami hazard assessment (Priest et al., 2008) (Figure 17). The two "average" simulations were run on a numerical grid developed from a DEM that reconstructs the paleotopography of Cannon Beach prior to urban development (e.g., simulation Average 9 is shown in Figure 19). To compare our results to velocities produced by a larger tsunami, Figure 17 also shows flow speeds from a third scenario, Large 14 (run 271), that simulates inundation on a grid that reflects the modern topography and incorporates artificial fill and other human modifications to the landscape. Complete explanations of the earthquake source parameters used for the simulations are presented in Priest et al. (2008).

Maximum flow speeds calculated by inundation modeling vary from less than 1 to over 7 m/s and unlike the TsuSedMod results, the simulations show significantly lower flow speeds at sites furthest inland (Figure 17). Flow speeds predicted by Average 9, the smallest tsunami simulation of the comparison, range from 2.5 to 3.2 m/s within 300 to 600 m of the beach. Sites further inland decrease to less than 2 m/s. Although still lower than our calculations, faster flow speeds predicted by the larger simulation, Average 14, show a different trend that is similar to velocities predicted by TsuSedMod (Figure 17). In both cases the flow speed calculated for core 14 at 600 m is higher than the flow speeds calculated for cores 8 and 11 located about 300 m from the beach. However, unlike the TsuSedMod results, the simulated flow speeds for Average 14 at sites over 800 m inland decrease markedly to values below 2 m/s similar to the Average 9 scenario. Flow speeds for the simulation Large 14 show trends in flow speed variation that are similar to Average 14. However, in two cases, cores C and 14, the flow speeds predicted by the simulations are in very close agreement to flow speeds calculated by TsuSedMod. Decreasing flow speeds between core C (300 m) and cores 8 and 11 (305 to 315 m) in Pompey Marsh (Figure 2) present another trend common to all sets of flow speed data. Among these independent data sets there appears to be some similarities in the trends of flow speed variation from one core site to another, but in all cases the flow speeds calculated by TsuSedMod are higher than flow speeds determined from inundation modeling. We do not know if these differences indicate an over-estimation of flow speeds by the sediment model or under-

estimation by the simulations, or whether any of the calculations accurately reflect the actual velocities produced by the 1700 tsunami.

Compared to flow speeds estimated for historical tsunamis, our flow speed calculations for the 1700 Cascadia tsunami are much lower. For the 1993 Hokkaido-Nansei-Oki tsunami, Titov and Synolakis (1997) estimated the velocity of flow over the Aonae peninsula at 10 to 19 m/s, which is consistent with 10 to 18 m/s field estimates of Shimamato et al. (1995). Flow speeds for the 1998 Papua New Guinea tsunami, estimated at 16 to 17 m/s within 100 m of the shoreline (Titov et al, 2001; Kawata, 1999), also exceed our velocity estimates.

DISCUSSION

MODELING ASSUMPTIONS

We present flow speed estimates for the 1700 tsunami derived from calculations using a simple sediment transport model that operates under several assumptions. Recognizing that this is the first attempt to reconstruct the flow parameters of a prehistoric tsunami using TsuSedMod, we endeavor to evaluate the effectiveness of the model, assess its strengths and weaknesses, and recommend further areas of improvement and application. The model's primary assumption requires that sediment suspended in the water column is in equilibrium with the steady, long-period uniform uprush of the tsunami wave and that spatial decelerations in the flow are negligible (Jaffe and Gelfenbaum, 2007). Other caveats about our modeling approach involve the difficulty in correlating individual sand layers among the core sites and the unequal treatment of bottom friction used by tsunami inundation models. Questions raised by the analyses include: What are the effects of topography? And, in the comparisons between flow speeds calculated by TsuSedMod and maximum velocities predicted by tsunami simulations, are we comparing apples with apples?

Without knowing the actual flow speeds of the 1700 tsunami, in the following discussion we cautiously evaluate the model's performance by offering simple explanations that may account for significant trends and apparent inconsistencies in the data. We may never completely validate or rule out these results, but the merit in our approach is that it derives the flow speed of the 1700 tsunami from field and laboratory measurements on sand layers deposited by the actual waves that inundated Cannon Beach. As a result, our approach provides a means to estimate prehistoric tsunami flow parameters that is completely independent of numerical inundation models. The following sections discuss the several caveats and assumptions involved in our approach and their implications on the modeling results. In consideration of these issues, we recommend new directions in the application of sediment transport models and possible improvements.

CONVERGENCES IN SEDIMENT TRANSPORT AND TOPOGRAPHIC EFFECTS

Sediment transport model calculations indicate an increase in flow speed from 6.5 m/s at Pompey Marsh to over 8.7 m/s at cores 45 and X (Figure 17), located about 0.9 and 1.2 km up the valley, respectively. Does this trend reflect the actual acceleration of the 1700 tsunami as it inundated the lower Ecola Creek valley or does the data reflect some other process that violates key assumptions of the model? If the flow speed estimates for locations near the distal reach of

the tsunami deposit are inaccurate as suggested by tsunami simulations, then an alternative hypothesis is that the deposits formed from some process other than suspended sediment settling out of the water column. Tsunami deposits at Arop, Papua New Guinea, studied by Gelfenbaum and Jaffe (2003), were used to calculate flow speeds for the 1998 tsunami. Jaffe and Gelfenbaum (2007) speculated that strong deceleration in tsunami flow near the inland extent of inundation may have caused a greater component of the suspended load to drop out of suspension, creating a convergence in sediment transport. Alluding to this process, they reasoned that rapid deceleration in flow landward of 600 m at Arop may have produced coarser and thicker deposits that, when used as inputs to TsuSedMod, likely over-predicted the speed of the tsunami.

Three observations suggest that this scenario may apply to calculations at Cannon Beach. First, we note that the grain size distributions for samples from the two distal sites (cores 45 and X) are the least consistent with deposition from a suspended sediment load (Figure 12), which implies the sand layers were deposited by some other process. Second, cores 45 and X are located greater than 0.8 km up the valley near the location where the furthest landward deposits of the 1700 tsunami have been detected (Figure 6). And third, both sites are located within tens of meters of the valley margin, which may have acted as a backstop preventing steady, uniform flow. A convergence in sediment transport near the landward limit of the mapped deposits, possibly related to decelerating tsunami flow, provides a reasonable explanation for the higher flow speeds calculated by TsuSedMod. We suspect that sand deposits beyond 0.8 km inland may reflect non-uniform flow conditions as the 1700 tsunami rapidly decelerated in speed upon reaching the valley margin, thus violating key model assumption of steady, uniform flow.

Alternatively, the topography of a constricting valley that decreases in width landward may create a funneling effect that causes the tsunami flow to thicken or accelerate inland. While this hypothesis may explain landward increasing flow velocities for special geographic features such as steep narrow valleys or where the terrain slopes downward in the direction of wave inundation (e.g. Titov and Synolakis, 1997), tsunami simulations for Cannon Beach are not consistent with this scenario. For example, inundation modeling by Priest et al. (2007) predicts slower velocities 0.8 to 1.2 km inland, which conflicts with the higher flow speeds calculated by the sediment transport model.

Variations in calculated flow speed (Figure 17) at some sites may reflect their proximity to the channel of Ecola Creek. Similar flow speeds determined for cores C and 14 (7.6 to 7.4 m/s, respectively), two sites close to the creek channel, exceed flow speeds calculated for cores 8 and 11, located in the southern part of Pompey Marsh and farther from the creek. There are two possible explanations that support this observation. First, tsunami flow focused by the channel may produce higher flow speeds near the channel and lower flow speeds as the wave flows south into Pompey Marsh, away from the channel. A second possibility consistent with tsunami simulations is that after the tsunami inundates the mouth of the creek, the incoming wave reflects off of the northeastern wall of the valley and is directed toward Pompey Marsh with flow speeds decreasing from north to south. Review of computer animations of selected tsunami simulations for Cannon Beach show waves reflecting off the valley wall and suggest this may play a role in sediment transport.

SAND LAYER CORRELATION

Careful attention to stratigraphic features in the sediment cores lends confidence to correlations of sand deposits left by the 1700 tsunami and other tsunami events in the past 1500 years at Cannon Beach (Figures 7 and 8; Witter, 2008). Some of the evidence includes the consistent depth of the deposit around 0.4 to 0.6 m below the marsh surface, its sharp contact over distinctive black peat and the presence of clean, quartz-rich sand resembling beach sediment (Figure 11). Individual, normally-graded layers within the deposit, however, were more difficult to correlate with such certainty. Table 3 lists the various sand beds that show apparent evidence of normal grading based on field observations. Multiple sand beds in a tsunami deposit have been interpreted to reflect multiple waves generated by a single earthquake (Peters et al., 2007). The deposit in core C includes three such beds, some cores had two beds (cores 11 and 45) and the others had none (Figure 11). Closer examination of subsamples of the deposits in the laboratory (Table 3) revealed both normally- and reversely-graded layers within some beds (e.g., core 45, 57.5-62 cm). Other beds were reversely graded (e.g., core 11, 39-40.5 cm). To select the most appropriate layers to use for model inputs, we chose the lowest layers in each deposit that displayed normal grading consistent with settling out of suspension (Figure 12b). Despite this procedure, specific sand layers to which the model has been applied may not correlate from one core to the next because of erosion by successive tsunami waves or return flow, or from local variations in the sediment supply.

FLOW SPEEDS ESTIMATED BY INUNDATION MODELING

Comparisons between flow speeds calculated by TsuSedMod and maximum flow velocities determined from tsunami simulations involve many assumptions. Are we comparing apples and oranges? For instance, Cannon Beach tsunami simulations using the inundation model SELFE (Zhang et al., 2007; Zhang and Baptista, 2008) incorporate zero bottom friction, whereas TsuSedMod calculates bed roughness as a function of the Nikuradse bed roughness (Nikuradse, 1933) and the roughness contributed by saltating sediment. Bottom friction affects the wave evolution of tsunamis flowing overland (Titov and Synolakis, 1997), however, an appropriate coefficient of friction is difficult to estimate and results of tsunami studies suggest that inundation models may be relatively insensitive to the roughness coefficient (Kobayashi et al., 1987, Zelt, 1991, Kobayashi, and Wurjanto, 1992, Liu et al., 1995). Because the two approaches treat bottom friction unequally, the differences evident in the comparisons are possibly manifestations of the different ways the two models account for bottom friction and bed roughness.

In our application, TsuSedMod calculates maximum flow speed using flow depths specified from selected tsunami simulations for Cannon Beach (Priest et al., 2008). The flow depths derived from the inundation model represent maximum flow depths observed over two to four hours over the course of the simulation. However, maximum flow depth usually does not coincide with maximum flow speed. Therefore, future applications of the model that constrain flow depth with inundation models should sample water depth at the time step when the flow reaches its peak velocity. The effect on flow speed may be negligible if the flow depth at peak velocity is over 2 m. However, because sediment model calculations of flow speed are sensitive to changes in flow depth at lower values, water depths less than 2 m at peak velocity may result in considerably higher flow speeds.

We lack topographic maps of the landscape that was inundated by the 1700 tsunami. Ground penetrating radar surveys imply a long-lived barrier ridge (Peterson et al., 2008), but other aspects of the landscape, like the height of the foredune and the configuration of the creek mouth, are impossible to reconstruct. Two of the tsunami simulations used to estimate flow depth (Average 9 and 14) were run on a numerical grid developed from a digital elevation model (DEM) that was modified to represent the landscape 1000 years ago. The purpose of the reconstruction was to compare the extent of inundation predicted by tsunami simulations to the total mapped extent of a sand sheet deposited by a Cascadia tsunami about 1000 years ago (Witter, 2008). The reconstructed terrain model removes artificial fills like the road embankment for U.S. Highway 101 and dikes placed to impound waste-water ponds. The DEM also accounts for erosion of the coastal dunes and bluffs and approximately 1 m of sedimentation in the lower Ecola Creek valley. We lacked sufficient resources to construct a similar paleolandscape for the 1700 tsunami simulation. A third simulation (Large 14) used in the comparison of flow speeds (Figure 17) was run on a grid developed from modern topography. Differences in the flow speeds estimated by these simulations reflect the effects of these obvious topographic inconsistencies not present in the 1700 landscape. For example, the paleolandscape has a coastline 70 m seaward of the modern coastline, reflecting 1000 years of estimated erosion. The 1700 coastline was probably much closer to the modern shoreline.

CONSTRAINTS ON FLOW DEPTH

Although, we derive flow depths from tsunami simulations for Cannon Beach, there are alternative approaches that can be used to constrain tsunami flow depth. For instance, Froude numbers are determined by the ratio of the tsunami flow speed to the wave speed, $\frac{U}{\sqrt{gh}}$, which is a function of flow depth (Figure 16). As we gain a better understanding of the variability of Froude numbers in nature, they may enable us to constrain tsunami flow depth as well as speed from the character of their deposits (Jaffe and Gelfenbaum, 2007). For example, the results of experimental (Yeh et al., 1989) and field studies (Kawata, 1999) suggest that Froude numbers between 1 and 2 may be appropriate to constrain flow depths for tsunamis. If this is a realistic range, then these Froude numbers bracket flow depths that vary between about 1 to 7 m in Figure 16, which correspond to a range of flow speeds from >6 to 9 m for the 1700 tsunami.

Flow depths are difficult to derive from the distribution of prehistoric tsunami deposits alone and few estimates come from geologic data. Peterson et al. (2008) attempted to reconstruct minimum runup estimates at the open coast for Cascadia tsunamis from the distribution of sand deposits in the lower Ecola Creek valley. Their interpretation that the 1700 tsunami did not overtop a 6-m-high (NAVD 88) stable barrier ridge comes from inferred tsunami flow paths interpreted from the distribution of sand deposited by the wave. Furthermore, stratigraphic reconstructions of the extent of the 1700 tsunami deposit by Witter (2008) showed a more extensive distribution of the sand sheet than that mapped by Peterson et al. (2007). Lacking conclusive data on the runup elevation of 1700 tsunami, Witter speculated that it probably did overtop the foredune at Cannon Beach from the simple reasoning that the 1964 Alaska tsunami nearly overtopped the ridge and the 1700 tsunami likely produced higher runups based on the much greater extent of its deposits (Figure 6). Regardless of the actual runup elevation at the foredune, geologic estimate of tsunami

runup do not reflect actual flow depths at the various sites used for modeling sediment transport. Tsunami simulations (e.g., Figure 18) show that flow depth varies by several meters from site to site and do not equate with runup at the open coast.

We have no independent way of verifying that any of the earthquake source models used for the three tsunami simulations correspond to the 1700 earthquake. The Average 14 and Average 9 scenarios use ~18 m of slip, while the "large" scenario uses ~26 m of slip on the subduction zone (Priest et al., 2008). Satake et al. (2003) inferred average slip of ~19 m from inversion of 1700 tsunami runup data in Japan. Coastal subsidence predicted from the fault dislocation models for the "average" tsunami scenarios have a somewhat better match to the 1700 coastal subsidence data of Leonard et al. (2004) than subsidence for the Large 14 scenario, but there are many uncertainties in the Leonard et al. data (Priest et al., 2008). The Average 14 and Large14 earthquake scenarios partition slip to a splay fault, while the Average 9 rupture places all slip on the megathrust. Greater seafloor uplift for scenarios that involve rupture of a splay fault results from higher splay fault dip compared to the megathrust, but coastal subsidence is unaffected, so the Leonard et al. (2004) data cannot be used to test the models (Priest et al., 2008). Turbidite data used to infer relative size of earthquakes suggest that the 1700 earthquake was an "average" Cascadia event (Priest et al., 2008), but it is hard to translate this qualitative inference into a detailed source model.

RECOMMENDATIONS FOR FUTURE MODELING

Taking together the assumptions of the sediment transport model and the caveats on how we have applied it to reconstruct the flow speed of the 1700 Cascadia tsunami at Cannon Beach, we offer the following recommendations for future studies:

(1) Future investigations should focus on sites with simple topographic settings to avoid convergences in flow that may violate model assumptions. Tsunami simulations for Cannon Beach show that event the relatively simple geography and low-relief of the lower Ecola Creek valley produces complicated flow dynamics, including flow deceleration and wave reflection that may lead to spatial convergences in sediment transport.

(2) We recommend studies that couple sediment transport models with tsunami inundation models to more completely explore the hydrodynamic parameters that can be gleaned from tsunami deposits. Particular emphasis should be placed on estimating realistic Froude numbers for tsunamis that may help constrain both the speed and depth of prehistoric tsunamis.

(3) How critical is the zero friction assumption used by the inundation model? What are the effects of vegetation, buildings and other topographic features on overland flow? We recommend wave tank experiments designed to better define realistic values for bottom friction and bed roughness used in tsunami inundation models.

(4) Finally, we plan to further refine our modeling at Cannon Beach by applying the following steps to improve comparisons between the sediment transport model results and the flow parameters predicted by tsunami simulations:

a. Specify the flow depths for each sample site at same time step as the maximum velocity for each tsunami simulation.
b. Run simulations on a paleolandscape more closely resembling that of 1700.
c. Run SELFE in 3-D mode to better simulate tsunami flow velocity and depth.

SUMMARY AND CONCLUSIONS

Cannon Beach, Oregon faces several hazards from flooding by extreme ocean levels. Severe winter storms and large floods by Ecola Creek may occur several times every decade. However, tsunamis generated by both distant and local sources present the most serious risks. In 1964 a tsunami generated by the M 9.2 Prince William Sound earthquake in Alaska struck the Pacific coast of the western U.S., flooding Cannon Beach and other coastal communities in Oregon. But much greater waves inundated Oregon's coastline 264 years earlier when a M 9 earthquake ruptured the Cascadia subduction zone in 1700. Lasting effects of the 1700 tsunami include an extensive sand sheet deposited in the lower Ecola Creek valley by ocean flooding. In an effort to increase our understanding of the hydrodynamic aspects of the tsunami waves, we present the first application of a simple sediment transport model, TsuSedMod (Jaffe and Gelfenbaum, 2007), that reconstructs the flow speed of the 1700 tsunami based on the thickness and grain size of sand layers deposited by the wave.

TsuSedMod calculates tsunami flow speed from the shear velocity necessary to suspend the quantity and grain size distribution of the observed sand layers. The model assumes that sediment is suspended by a steady, spatially uniform current during the peak tsunami flow and the sediment settles out of suspension at maximum inundation when the flow speed decreases to zero. Sand deposits that record the 1700 tsunami were sampled in the field and analyzed at the USGS Sedimentology Lab in Menlo Park to determine layer thickness and grain size distributions. For model inputs, we selected individual layers near the base of each deposit that exhibited normal grading consistent with a deposit formed by suspended sediment that settled out of the water column.

Sensitivity tests indicate that calculated flow speeds are variously sensitive to the model parameters considered, including bed roughness, the resuspension coefficient and flow depth. TsuSedMod is particularly dependent on flow depth when water depths decrease below about 2 m. Considering all the sensitivity analyses and assuming the parameters used represent realistic values found in nature, speeds estimated for the 1700 tsunami range from about 5 to 9 m/s.

Flow speed estimated for the 1700 tsunami using flow depth inputs specified by tsunami simulations range from 6.5 to 8.8 m/s. Sediment samples that provide thickness and grain size inputs come from sites located 300 to over 1200 m inland from the beach. Higher flow speeds are calculated for sites furthest landward, contrary to maximum flow velocities predicted by tsunami inundation models. For comparison, maximum flow speed predicted by the simulations vary from less than 1 to over 7 m/s and show a significant decrease in velocity at the two sites furthest inland. Similarities in the trends of flow speed variations among sites near the beach demonstrate some consistencies in the results of the different modeling methods, however, flow

speeds calculated by TsuSedMod were higher than velocities predicted by the tsunami simulations in all cases.

Convergences in sediment transport offer possible explanations for the higher flow speeds predicted for the two sites furthest inland. Sudden deceleration in spatial flow, perhaps influenced by rapid waning of the tsunami as it reached the inundation limit or caused by the wave interacting with the steep, southeastern margin of the valley, may have concentrated sediment deposited at cores 45 and X. Grain size distributions of sand layers from these sites indicate that processes other than, or in addition to, settling of suspended sediment are responsible for the deposit. Based on these observations, we infer that flow speeds of >8 m/s over-estimate the actual velocity of the 1700 tsunami near the distal reaches of its deposit.

The results of this study raise several important questions that should be addressed by future research. For instance, is it appropriate to compare flow speeds calculated by sediment transport models to velocities predicted by inundation modeling if they operate under different assumptions? How dependent is flow speed on topography, particularly when digital elevation models must be modified to reconstruct the ancient landscape? Do we understand the natural variability of Froude numbers well enough to use them as constraints on tsunami flow depth? Future applications of TsuSedMod on prehistoric tsunami deposits should focus on sites with low topographic relief and simple geography that harbor extensive sand sheets deposited by prehistoric tsunamis. Considerable insights may be gained by coupling tsunami sedimentation models with inundations models to more completely examine the hydrodynamic flow parameters that can be derived from tsunami deposits.

ACKNOWLEDGMENTS

Bruce Jaffe (USGS) trained Witter in the use of the sediment transport model, TsuSedMod, and provided critical guidance throughout the entire modeling process. Without his open collaboration, this project would not have been possible. We are grateful to Mike Torresan, Gary Schneider and Angela Lam for training and assistance with particle size analysis at the USGS Menlo Park Sedimentology Laboratory. Yuki Sawai (Geological Survey of Japan), generously contributed analyses of fossil diatoms that aided in paleoecological interpretations. The U.S. Geological Survey's National Earthquake Hazards Reduction Program (award number 07HQGR0089) supported this investigation.

REFERENCES

Abramson, H.F., 1998. Evidence for tsunamis and earthquakes during the last 3500 years from Lagoon Creek, a coastal freshwater marsh, northern California [MS thesis]. Humboldt State University, 76 pp.

Atwater, B.F., 1987, Evidence for great Holocene earthquakes along the outer coast of Washington state: Science, v. 236, p. 942-944.

Atwater, B.F., and Hemphill-Haley, E., 1997, Recurrence intervals for great earthquakes of the past 3500 years at northeastern Willapa Bay, Washington: U.S. Geological Survey Professional Paper 1576, 108 p.

Atwater, B.F., Musumi-Rokkaku, S., Satake, K. Tsuji, Y., Ueda, K., Yamaguchi, D.K., 2005. The orphan tsunami of 1700—Japanese clues to a parent earthquake in North America, U.S. Geological Survey Professional Paper 1707, 133 p. (published jointly by University of Washington Press, Seattle).

Benson, B. E., Grimm, K. A., and Clague, J. J., 1997, Tsunami deposits beneath tidal marshes on northwestern Vancouver Island, British Columbia: Quaternary Research, v. 48, p. 192-204.

J.C. Borrero, 2005, Field Data and Satellite Imagery of Tsunami Effects in Banda Aceh , Science, v. 308, p. 1596.

Bourgeois, J., Petroff, C., Yeh, H., Titov, V., Synolakis, C.E., Benson, B., Kuroiwa, J., Lander, J., Norabuena, E., 1999. Geologic setting, field survey and modeling of the Chimbote, Northern Peru, tsunami of 21 February 1996. Pure and Applied Geophysics 154, 513–540.

Clague, J.J., Bobrowski, P.T., and Hutchinson, I., 2000, A review of Geological records of large tsunamis at Vancouver Island, British Columbia, and implications for hazard: Quaternary Science Reviews, v.19, p. 849-863.Dietrich, W.E., 1982. Settling velocity of natural particles. Water Resources Research 18 (6), 1615–1626.

Darienzo, M.E., and Peterson, C.D., 1990, Episodic tectonic subsidence of late Holocene salt marshes, northern Oregon central Cascadia margin: Tectonics, 9, No. 1, p. 1-22.

Drake, D.E. and Cacchione, D.A., 1989. Estimates of suspended sediment reference concentration (Ca) and resuspension coefficient ($\gamma 0$) from near-bottom observations on the California shelf. Continental Shelf Research 9 (1), 51–64.

Dunbar, C.K. and C. Weaver, 2007, U.S. states and territories national tsunami hazard assessment, historic record and sources for waves, *Eos Trans. AGU,* 88 (52), Fall Meet. Suppl., Abstract NS21A-08.

Gallaway, P.J., Peterson, C.D., Watkins, A.M., Craig, S., and McLeod, B.L., 1992, Paleo-tsunami inundation and runup at Cannon Beach, Oregon, Final Report to Clatsop County Sheriff's Office, Oregon, Unpublished report, 47 p.

Gelfenbaum, G. and Jaffe, B., 2003. Erosion and sedimentation from the 17 July, 1998 Papua New Guinea tsunami. Pure and Applied Geophysics 160, 1969–1999.

Gelfenbaum, G. and Smith, J.D., 1986. Experimental evaluation of a generalized suspended sediment transport theory. In: Knight, R.J., McLean, J.R. (Eds.), Shelf Sands and Sandstones. Memoir, vol. 11. Canadian Society of Petroleum Geologists, pp. 133–144.

Goldfinger, C., Nelson, C.H., and Johnson, J., 2003, Holocene Earthquake Records From the Cascadia Subduction Zone and Northern San Andreas Fault Based on Precise Dating of Offshore Turbidites: Annual Reviews of Geophysics, v. 31, p. 555-577.

Hemphill-Haley, E., 1995, Diatom evidence for earthquake-induced subsidence and tsunami 300 yr ago in southern coastal Washington: Geological Society of America Bulletin, v. 107, p. 367-378.

Horning, T., 2006, Appendix C. Summary of eyewitness observations from 1964 Alaska tsunami in Seaside, Oregon, *in* Tsunami Pilot Study Working Group, Seaside, Oregon tsunami pilot study – Modernization of FEMA flood hazard maps, National Oceanic and Atmospheric Administration OAR Special Report: Seattle, Washington, NOAA/OAR/PMEL, p. C1-C7.

Jaffe, B.E. and Gelfenbaum, G., 2007, A simple model for calculating tsunami flow speed from tsunami deposits, Special Issue on Tsunami Deposits, Sedimentary Geology, v. 200, p. 347-361.

Kawata, Y., 1999. Field survey on the 1998 tsunami in northwestern area of Papua New Guinea. Report for Grant-Aid for Scientific Research (B)(1). Ministry of Education, Science, Sports and Culture, Japan. 81 pp.

Kelsey, H.M., Nelson, A.R., Hemphill-Haley, E., and Witter, R.C., 2005, Tsunami history of an Oregon coastal lake reveals a 4600 yr record of great earthquakes on the Cascadia subduction zone: Geological Society of America Bulletin, v. 117, no.7/8, p. 1009-1032.

Kobayashi, N., Otta, A.K. and Roy, I., Wave reflection and runup on rough slopes, *J. Waterways, Port, Coastal and Ocean Eng.* ***113*** (3), 282, 1987.

Kobayashi, N., and Wurjanto, A., Irregular wave setup and run-up on beaches, *J. Waterways, Harbors, Port, Coastal and Ocean Eng.* ***118*** (4), 368, 1992.

Krammer, K., and Lange-Bertalot, H., 1991a, Bacillariophyceae 3, Centrales, Fragilariaceae, Eunotiaceae. In Ettl, H., Gerloff, J., Heynig, H., and Mollenhauer, D., (eds), Süsswasserflora von Mitteleuropa, vol. 2, no. 3. Fischer, Stuttgart.

Lander, J.F., P.A. Lockridge, and M.J. Kozuch, 1993, Tsunamis affecting the West Coast of the United States, 1806-1992, KGRD No. 29: Boulder, Colorado, National Oceanic and Atmospheric Administration, National Geophysical Data Center, 242 p.

Lay, T., Kanamori, H., Ammon, C., Nettles, M., Ward, S., Aster, R., Beck, S., Bilek, S., Brudzinski, M., Butler, R., DeShon, H., Ekström, G., Satake, K., Sipkin, S., 2005, The Great Sumatra-Andaman Earthquake of December 26, 2004, Science, 308, 1127–1133, doi:10.1126/science.1112250.

Leonard, L. J., Hyndman, R. D., and Mazzotti, S., 2004, Coseismic subsidence in the 1700 Great Cascadia earthquake: Coastal estimates versus elastic dislocation models: Geological Society of America Bulletin, v. 116, p. 655-670.

Liu, P., L-F., Cho, Y.-S., Briggs, M. J., Kanoglu, U., Synolakis, C.E., Runup of solitary waves on a circular island, *J. Fluid Mech.* ***302***, 259-285, 1995.

Ludwin, R.S., Dennis, R., Carver, D., McMillan, A. D., Losey, R., Clague, J., Jonientz-Trisler, C., Bowechop, J., Wray, J., and James, K, 2005, Dating the 1700 Cascadia Earthquake – Great Coastal Earthquakes in Native Stories: Seismological Research Letters, v. 76, no. 2, p. 140-148.

Nelson, S.A. and Leclair, S.F., 2006, Katrina's unique splay deposits in a New Orleans neighborhood: GSA Today, v. 16, p. 4-10.

Nikuradse, J., 1933. Strömungsgesetze in rauhen Röhren, VDI Forschungsh., 361. (English translation, Laws of flows in rough pipes, NACA Tech. Memo. 1292, 62 p., Natl. Advis. Comm. For Aeron., Washington, D.C., 1950.)

O'Donnell, T., 1996, Cannon Beach: A Place by the Sea: Portland, Oregon, Oregon Historical Society Press, 164 p.

Peters, R., Jaffe, B. and Gelfenbaum, G., 2007, Distribution and sedimentary characteristics of tsunami deposits along the Cascadia margin of western North America: Sedimentary Geology, v. 200, p. 372–386.

Peterson, C.D. K.M. Cruikshank, H.M. Jol, and R.B. Schlichting, 2008, Minimum runup heights of paleotsunami from evidence of sand ridge overtopping at Cannon Beach, Oregon, Central Cascadia Margin, U.S.A., Journal of Sedimentary Research, v. 78, p. 390–409.

Priest, G.R., Allan, J. C., Myers, E., Baptista, A.M., and Kamphaus, R., 2002, Tsunami hazard map of the Coos Bay Area, Coos County, Oregon: Oregon Department of Geology and Mineral Industries, Interpretive Map Series IMS-21, scale 1:12,000.

Priest, G.R., Baptista, A.M., Flück, P., Wang, K., Kamphaus, R.A., and Peterson, C.D., 1997a, Cascadia subduction zone tsunamis: Hazard mapping at Yaquina Bay, Oregon, Final technical report to the National Earthquake Hazard Reduction Program: Oregon Department of Geology and Mineral Industries Open-File Report O-97-34, 144 p.

Priest, G.R., Chawla, A., and Allan, J. C., 2003, Tsunami hazard map of the Alsea Bay (Waldport) area, Lincoln County, Oregon: Oregon Department of Geology and Mineral Industries, Interpretive Map Series IMS-23, scale 1:12,000.

Priest, G.R., Myers, E., Baptista, A.M., Kamphaus, R., Peterson, C.D., and Darienzo, M. E., 1997b, Tsunami hazard map of the Yaquina Bay area, Lincoln County, Oregon: Oregon Department of Geology and Mineral Industries, Interpretive Map Series IMS-2, scale 1:12,000.Titov, T.V. and C.E. Synolakis, 1997, Extreme Inundation Flows During the Hokkaido-Nansei-Oki Tsunami, Geophysical Research Letters, 24 (11), 1315-1318.

Priest, G.R., Wang, K., Zhang, Y., Goldfinger, C., Witter, R., Peterson, C.D., Cruikshank, K., Baptista, A.M., Seaton, C., and Turner, P., 2008, Semi-Probabilistic Tsunami Hazard Assessment for Cascadia Subduction Zone Earthquakes: Cannon Beach, Oregon: Oregon Department of Geology and Mineral Industries, Open-File Report O-08-XX.

Reimer, P.J., M.G.L. Baillie, E. Bard, A. Bayliss, J.W. Beck, C. Bertrand, P.G. Blackwell, C.E. Buck, G. Burr, K.B. Cutler, P.E. Damon, R.L. Edwards, R.G. Fairbanks, M. Friedrich, T.P. Guilderson, K.A. Hughen, B. Kromer, F.G. McCormac, S. Manning, C. Bronk Ramsey, R.W. Reimer, S. Remmele, J.R. Southon, M. Stuiver, S. Talamo, F.W. Taylor, J. van der Plicht, and C.E. Weyhenmeyer, 2004, IntCal04 Atmospheric radiocarbon age calibration, 26-0 ka BP, Radiocarbon, v. 46 p. 1029-1058.

Satake K., Shimazaki, K., Tsuji, Y., and Ueda, K., 1996, Time and size of a giant earthquake in Cascadia inferred from Japanese tsunami records of January 1700: Nature, 379, p. 246-251.

Satake, K., Wang, K., and Atwater, B.F., 2003, Fault slip and seismic moment of the 1700 Cascadia earthquake inferred from Japanese tsunami descriptions: Journal of Geophysical Research, v. 108, p. ESE 7-1 to 7-17.

Schlicker, H. G., Deacon, R.J., Beaulieu, J.D., and Olcott, G.W., 1972, Environmental geology of the coastal region of Tillamook and Clatsop Counties, Oregon: Oregon Department of Geology and Mineral Industries Bulletin 74, 164p., 18 maps.

Shimamato, T. et al., 1995, Field survey report on tsunami disasters caused by the 1993 Hokkaido earthquake, Pure Appl. Geophys.1, 44, (3/4), 665-692.

Spaeth, M.G. and Berkman, S.C., 1967, The Tsunami of March 28, 1964 as Recorded at Tide Stations, ESSA Technical Report Coast & Geodetic Survey 33: Rockville, Maryland, U.S. Department of Commerce, 86 p.

Stuiver, M., and P.J. Reimer, 1993, Extended ^{14}C data base and revised CALIB 3.0 14C Age calibration program, Radiocarbon, v. 35, p. 215-230.

Titov, V.V., and C. Synolakis, 1997, Extreme inundation flows during the Hokkaido-Nansei-Oki tsunami, Geophysical Research Letters, v. 24, n.11, p. 1315-1318.

Titov, V.V., Jaffe, B.E., Gonzalez, F.I., Gelfenbaum, G., 2001. Re-evaluating source mechanisms for the 1998 Papua New Guinea tsunami using revised slump estimates and sedimentation modeling, Proceedings of the International Tsunami Symposium, p. 389–396.

Titov, V.V., A.B. Rabinovich, H.O. Mofjeld, R.E. Thomson, and F.I. González, 2005, The global reach of the 26 December 2004 Sumatra Tsunami, Science, v. 309, 2045-2048, DOI: 10.1126/science.1114576.

Tsunami Pilot Study Working Group, 2006, Seaside, Oregon tsunami pilot study – Modernization of FEMA flood hazard maps, National Oceanic and Atmospheric Administration OAR Special Report: Seattle, WA, NOAA/OAR/PMEL, 92 p., 7 appendices.

Tuttle, M.P., Ruffman, A., Anderson, T., and Jeter, H., 2004, Distinguishing tsunami from storm deposits in eastern North America: The 1929 Grand Banks tsunami versus the 1991 Halloween storm: Seismological Research Letters, v. 75, p. 117-131.

Vincent, C.E., Hanes, D.M., Bowen, A.J., 1991. Acoustic measurements of suspended sand on the shoreface and the control of concentration by bed roughness. Marine Geology 96, 1–18.

Walsh, T.J., Caruthers, C.G., Heinitz, A.C., Myers, E.P.III, Baptista, A.M., Erdakos, G.B., and Kamphaus, R.A., 2000, Tsunami hazard map of the southern Washington coast: Modeled tsunami inundation from a Cascadia subducting zone earthquake: Washington Division of Geology and Earth Resources, Geologic Map GM-49.

Wieberg, P.L. and Rubin, D.M., 1989. Bed roughness produced by saltating sediment. Journal of Geophysical Research 94 (C4), 5011–5016.

Witkowski, A., Lange-Bertalot, H., and Metzeltin, D., 2000, Diatom Flora of Marine Coasts I. *In* Lange-Bertalot, H. (ed.), Iconographia Diatomologica, vol. 7. A.R.G. Gantner Verlag.

Witter, R.C., Kelsey, H.M. and Hemphill-Haley, E., 2001, Pacific storms, El Nino and tsunamis: competing mechanisms for sand deposition in a coastal marsh, Euchre Creek, Oregon. Journal of Coastal Research v. 17, p. 563–583.

Witter, R.C., Kelsey, H.M., and Hemphill-Haley, E., 2003, Great Cascadiea earthquakes and tsunamis of the past 6700 years, Coquille River estuary, southern coastal Oregon: Geological Society of America Bulletin, v. 115, p. 1289-1306.

Witter, R.C., 2008, Prehistoric Cascadia Tsunami Inundation and Runup at Cannon Beach, Oregon: Oregon Department of Geology and Mineral Industries, Open-File Report O-08-XX.

Yeh, H., Ghazali, A., Marton, I., 1989. Experimental study of bore runup. Journal of Fluid Mechanics 206, 563–578.

Zelt, J.A., The runup of nonbreaking and breaking solitary waves, Coastal Engineering, *Coastal Engineering* ***15***, 205-246, 1991.

Zhang, Y., and Baptista, A.M., 2008, An efficient and robust tsunami model on unstructured grids. Part I: inundation benchmarks: [submitted December 31, 2007] Pure and Applied Geophysics: Topical issue on Tsunamis, 22 p.

Zhang, Y. L., Baptista, A.M., Wang, K., Goldfinger, C., Witter, R., Priest, G., Peterson, C., and Cruikshank, K., 2007, Hydrodynamic simulations of historic tsunamis from the Cascadia subduction zone [abs.]: Portland, Oregon, Coastal Zone 2007.

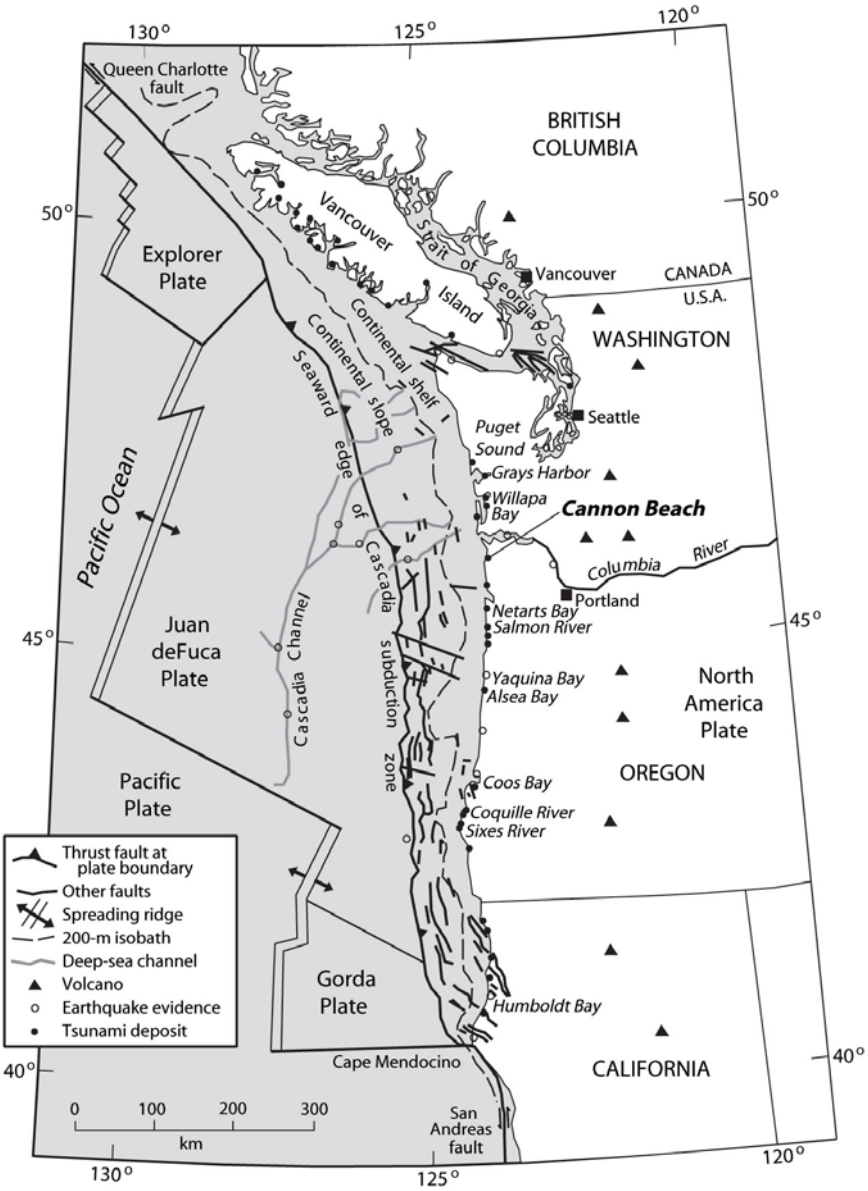

Figure 1 Tectonic setting of the Pacific northwestern U.S. showing the Cascadia subduction zone and other plate boundaries, Quaternary faults in the North American plate, and the location of the study site at Cannon Beach in northwestern Oregon (modified from Nelson et al., 2004). The deformation front (barbed line) is defined by bathymetry where the abyssal plain meets the continental slope and is inferred to represent the surface projection of the Cascadia thrust fault. Open and closed circles represent sites with evidence for prehistoric Cascadia earthquakes and tsunamis. Closed circles mark sites with deposits interpreted to record tsunami inundation caused by a M9 Cascadia earthquake on January 26, 1700 (Satake et al., 1996).

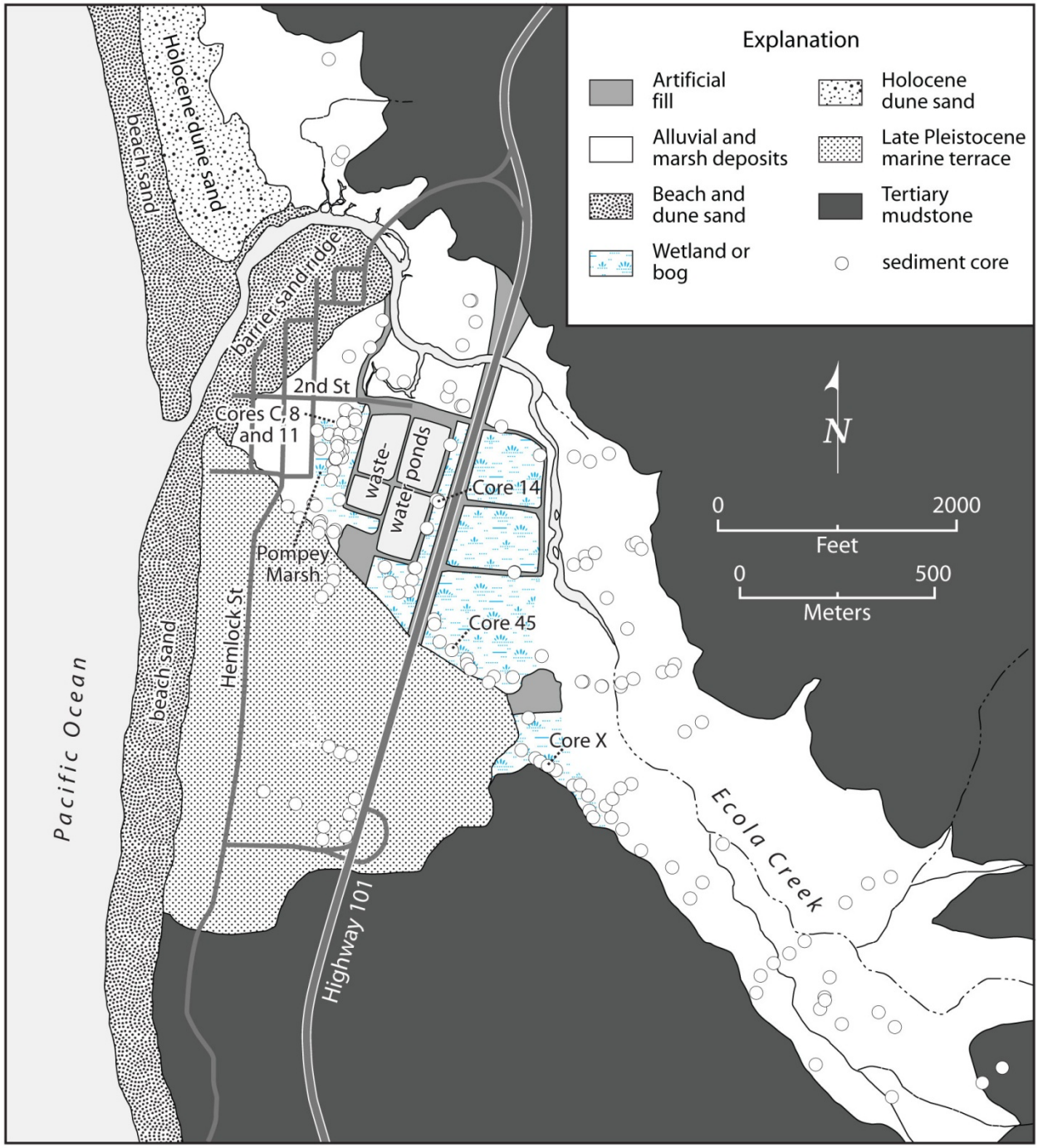

Figure 2 Map of the lower Ecola Creek valley and surrounding uplands showing the locations of 177 sediment cores examined for evidence of sand layers deposited by tsunamis or creek floods. Quaternary deposits in the valley and along the coast reflect the activity of both fluvial and coastal processes. The uplands surrounding Cannon Beach are chiefly composed of well-bedded mudstone of the middle to lower Miocene Cannon Beach member of the Astoria Formation (Niem and Niem, 1985).

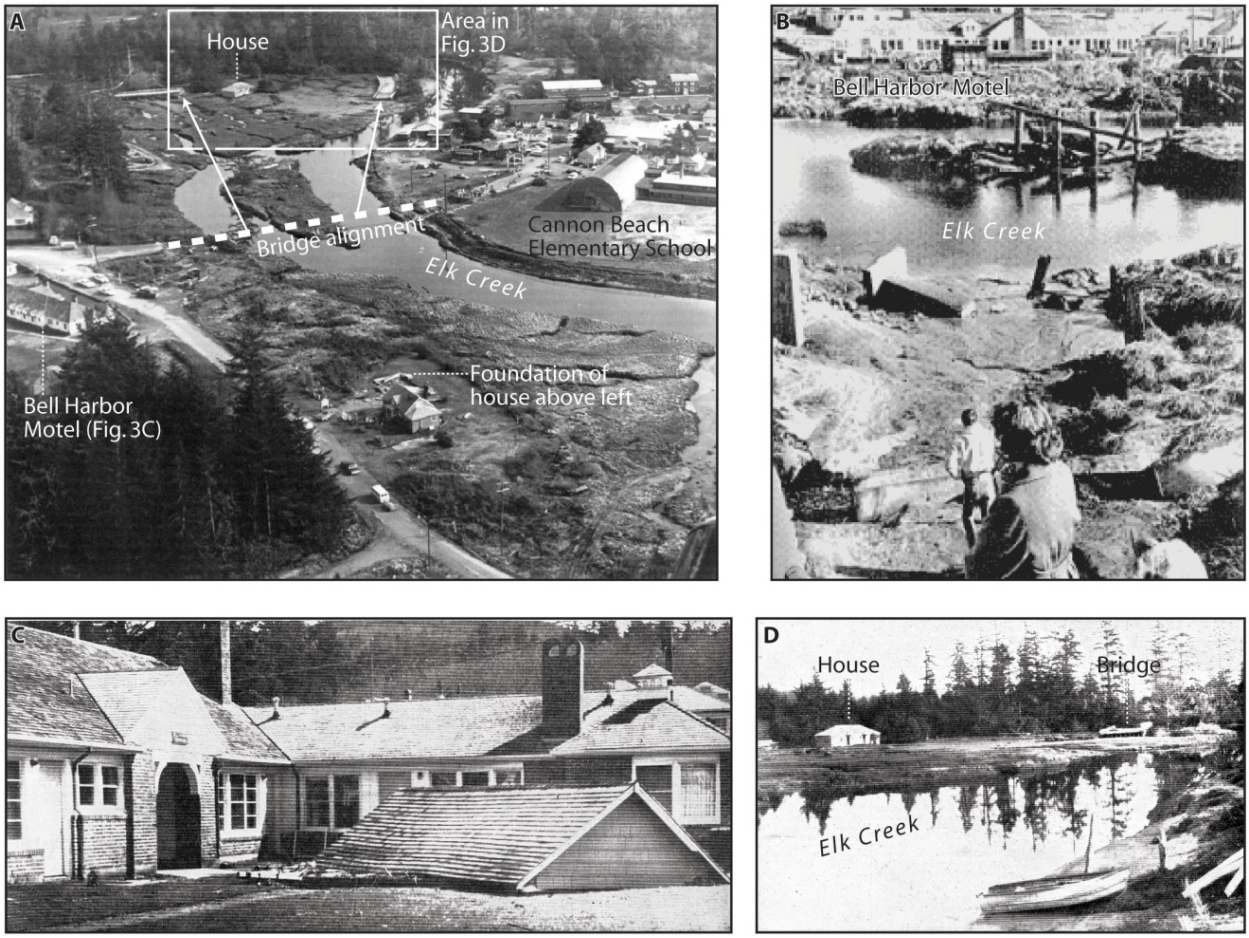

Figure 3 Photographs showing the impact of the 1964 Alaska tsunami (courtesy of the Cannon Beach Historical Society). (A) Oblique aerial photograph of the lower Elk Creek valley (now Ecola Creek) that flows through downtown Cannon Beach. Decking from the old Elk Creek bridge was torn from its abutments and transported 300 m upstream. A foundation in the lower part of the photo marks the original postition of a house that was carried 400 m upstream and deposited between the bridge sections. (B) View to the northwest across Elk Creek showing bridge pilings and piers, all that remain after the tsunami destroyed the Elk Creek bridge in 1964. Bell Harbor Motel can be seen in the distance across the creek. (C) The Bell Harbor Motel suffered considerable damage from flooding during the tsunami, including broken windows, water damage and destruction caused by drift logs. The roof of a different building was left in the front yard of the Motel after being carried several hundred yards by the waves. (D) View to the southeast looking across Elk Creek at the bridge remains and house transported hundreds of meter inland by the tsunami.

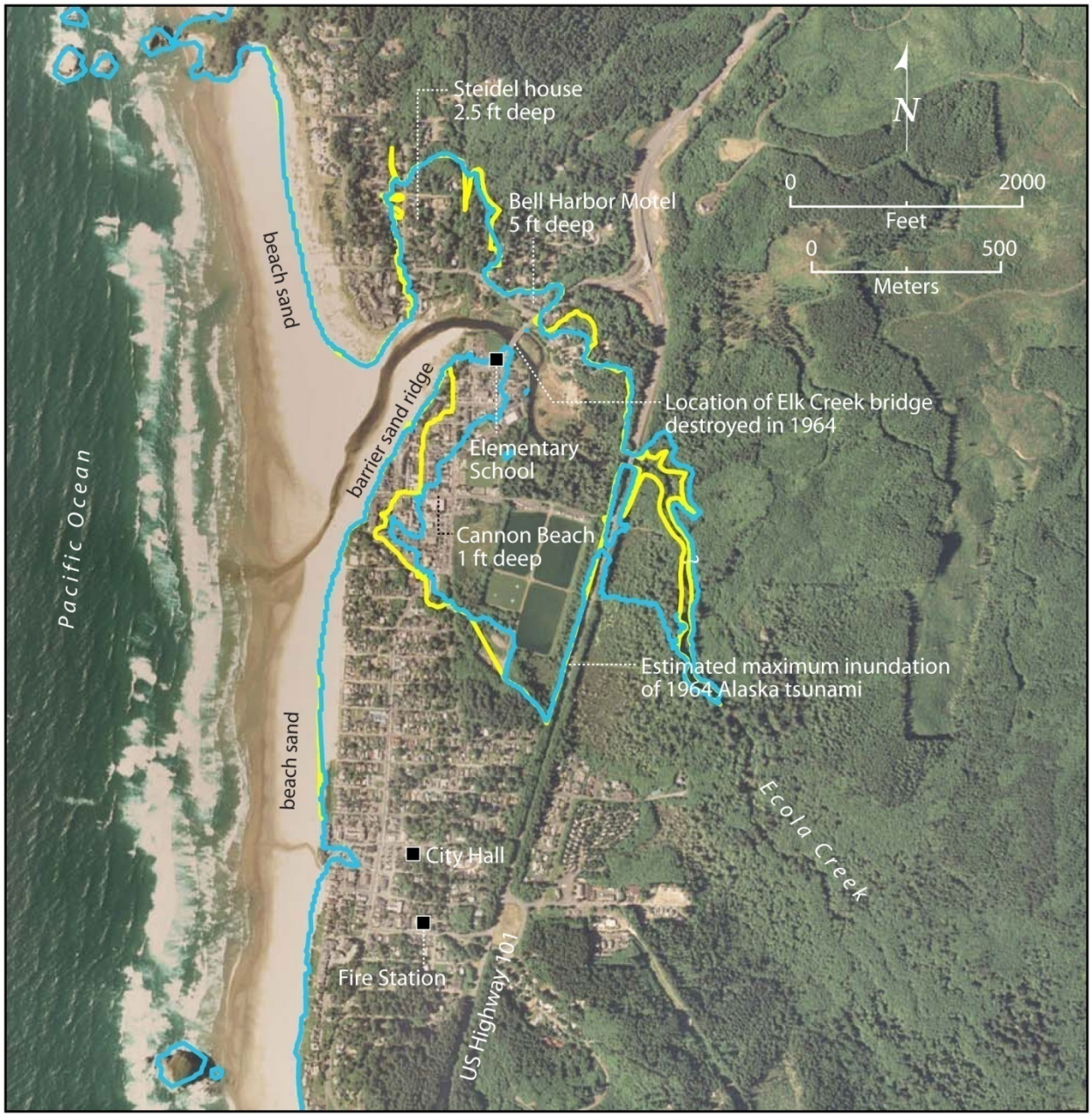

Figure 4 Color aerial orthophotograph of Cannon Beach in 2005 showing estimated maximum inundation of the 1964 Alaska tsunami (yellow dashed line) derived from eyewitness observations of water depth (Table 1) and 2-ft (0.6-m) contour lines from a digital elevation model provided by the City. The inundation line coincides with the 16-ft (4.9-m) contour line (NGVD 29) along the ocean front and north of Ecola Creek near the Steidel house and Bell Harbor Motel. The 10-ft (~3-m) contour line (NGVD 29) was used to approximate inundation in downtown Cannon Beach and east to US Highway 101. East of the highway the inundation line coincides with the 8-ft (2.4-m) contour line (NGVD 29) but there is no information from which to evaluate the extent of inundation in this area. Observations of the 1964 tsunami inundation were used in benchmark tests of numerical modeling employed to simulate the 1964 tsunami (shown by turquoise line).

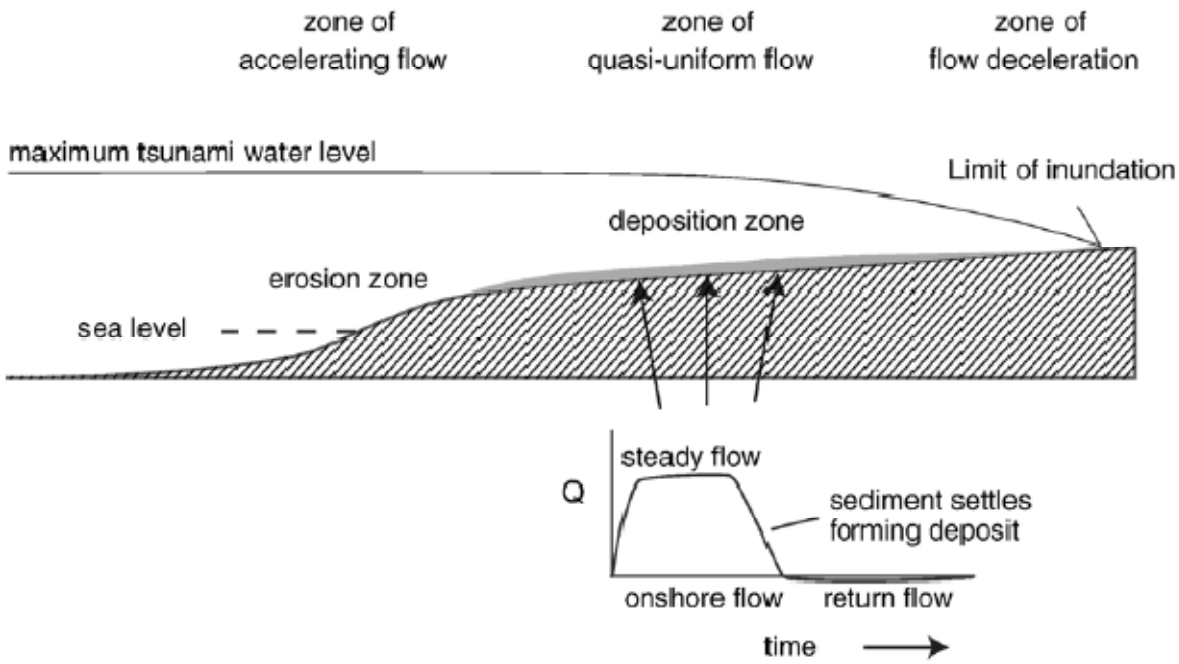

Figure 5 Conceptual model of tsunami sedimentation (Jaffe and Gelfenbaum, 2007). Deposit is formed in a zone of spatially quasi-uniform flow by sediment settling out of suspension when the tsunami flow speed goes to zero at the end of the onshore flow. Because the deposition zone is spatially quasi-uniform, the same temporal variation in flow speed applies to all locations in this zone. Quasi-uniform flow limits the amount of sediment deposited by sediment flux convergences, resulting in deposition from suspension being the primary process for tsunami deposit formation. The return flow is weak and concentrated in topographic lows and does not erode much of the deposit that formed during the onshore flow.

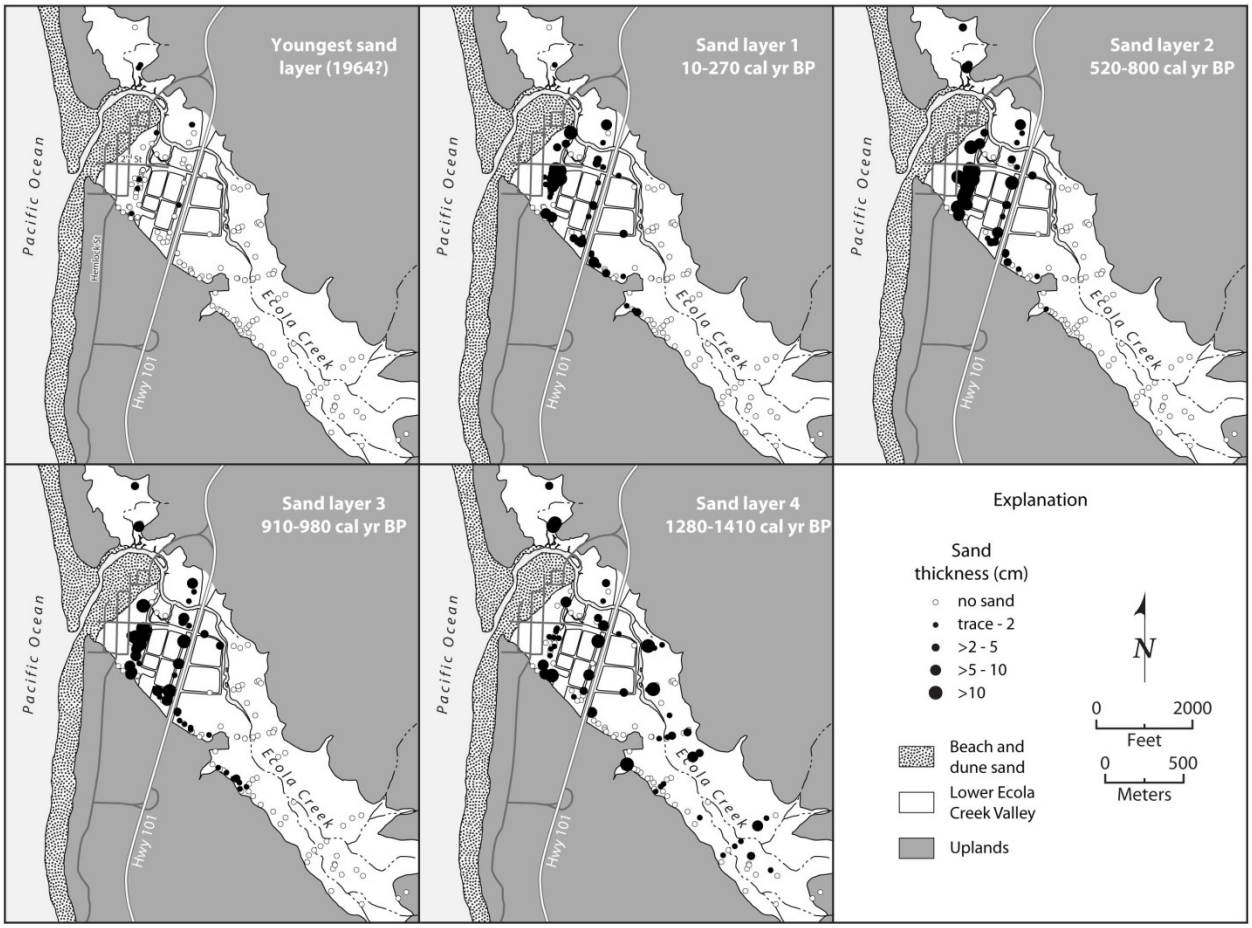

Figure 6 Maps of the lower Ecola Creek valley depicting the distribution of five sand deposits correlated among numerous sediment cores (black circles) and shown in stratigraphic profiles (Figs. 6–8) constructed from. Variations in the thickness of each sand layer is indicated by the diameters of black circles. Open circles show cores without a correlative sand layer. Calibrated ^{14}C ages are shown for each sand layer (Table 1); the youngest deposit may reflect deposition by the 1964 Alaska tsunami based on historical documents (see discussion in text).

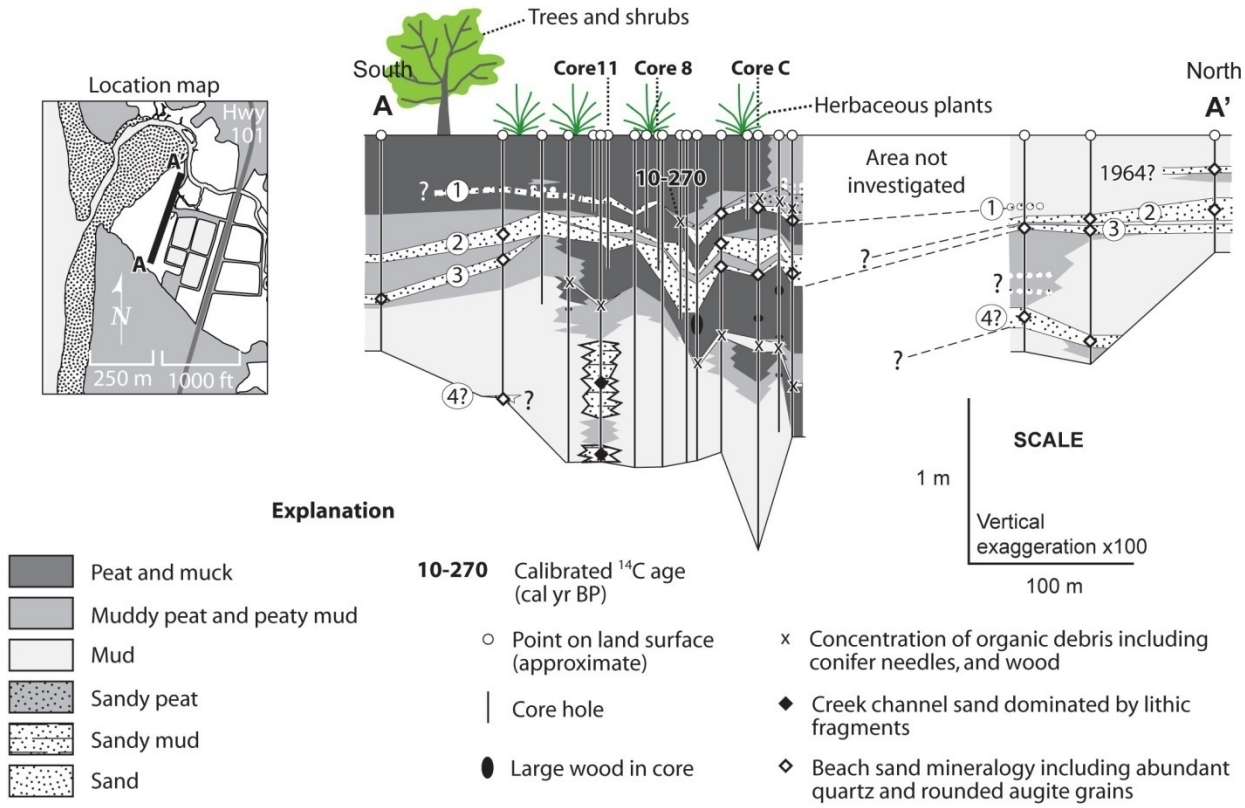

Figure 7 Stratigraphic profile A–A' showing five sand layers preserved beneath Pompey marsh near downtown Cannon Beach.

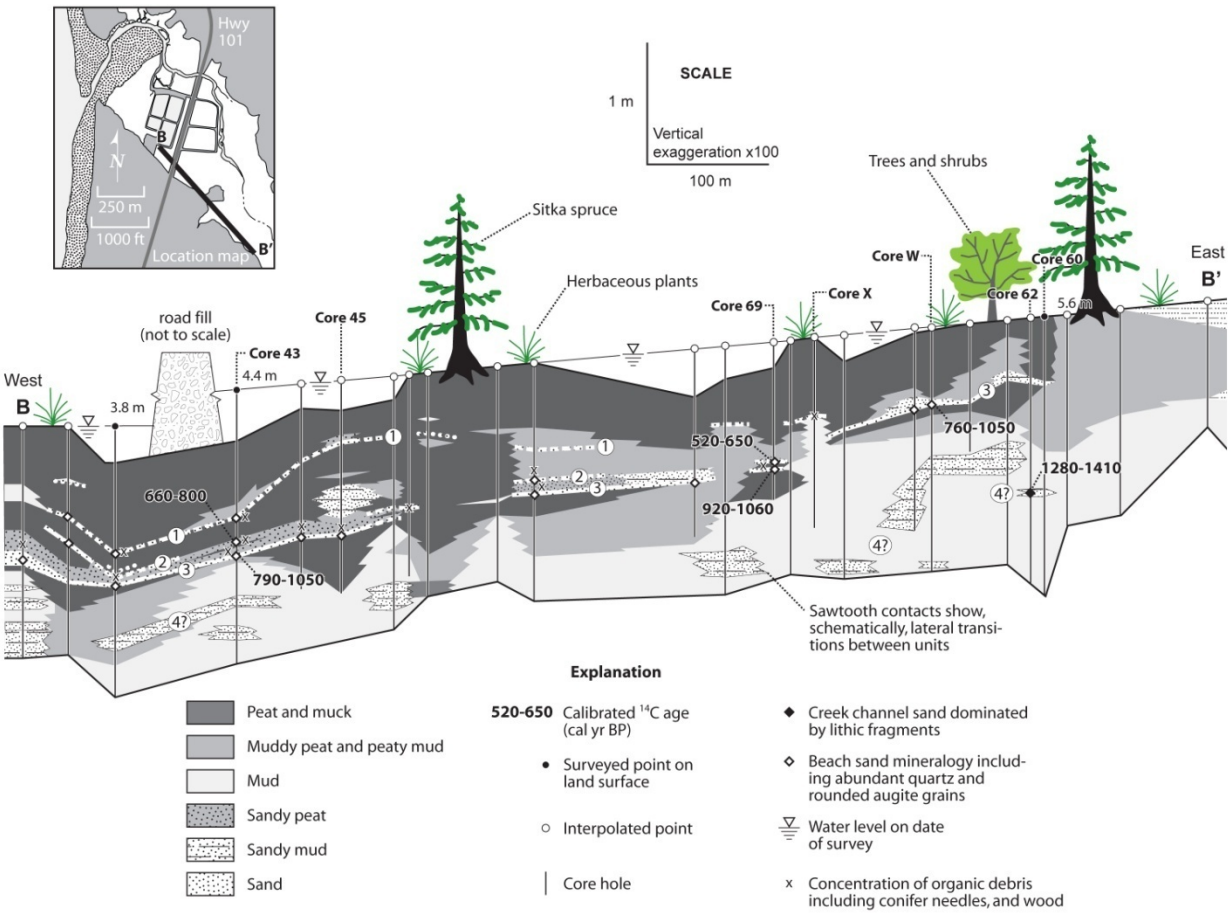

Figure 8 Stratigraphic profile B–B' showing four sand layers along the southeastern margin of the lower Ecola Creek valley.

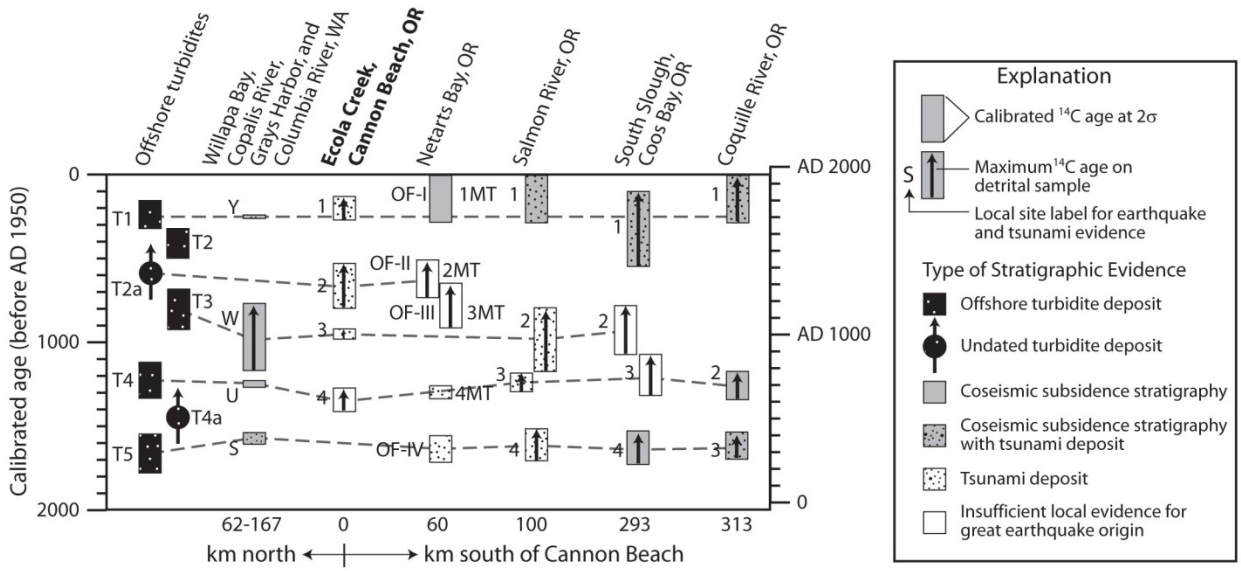

Figure 9 Comparison of calibrated ^{14}C ages and coastal evidence for great Cascadia earthquakes and tsunamis over the last two millennia at six sites in southwestern Washington and northwestern Oregon (modified from Nelson et al., 2004). Black rectangles represent ages for offshore turbidite deposits inferred to record strong shaking during prehistoric Cascadia earthquakes (from supplementary Table 2 in Goldfinger et al., 2007). Arrows indicate maximum limiting ^{14}C ages based on dates of detrital plant fossils. Ages for evidence at sites in southwestern Washington are from Atwater et al. (2003). Ages from coastal sites in Oregon come from Ecola Creek (Witter, 2008), Netarts Bay (Darienzo et al., 1994; Nelson et al., 1995; Shennan et al., 1997), Salmon River (Nelson et al., 1995, 2004), South Slough, Coos Bay (Nelson et al., 1996, 1998), and the Coquille River estuary (Witter et al., 2003). Local evidence for earthquake-related subsidence is lacking for one or more stratigraphic contacts at Ecola Creek, Netarts Bay and Coos Bay (e.g., Shennan et al., 1997).

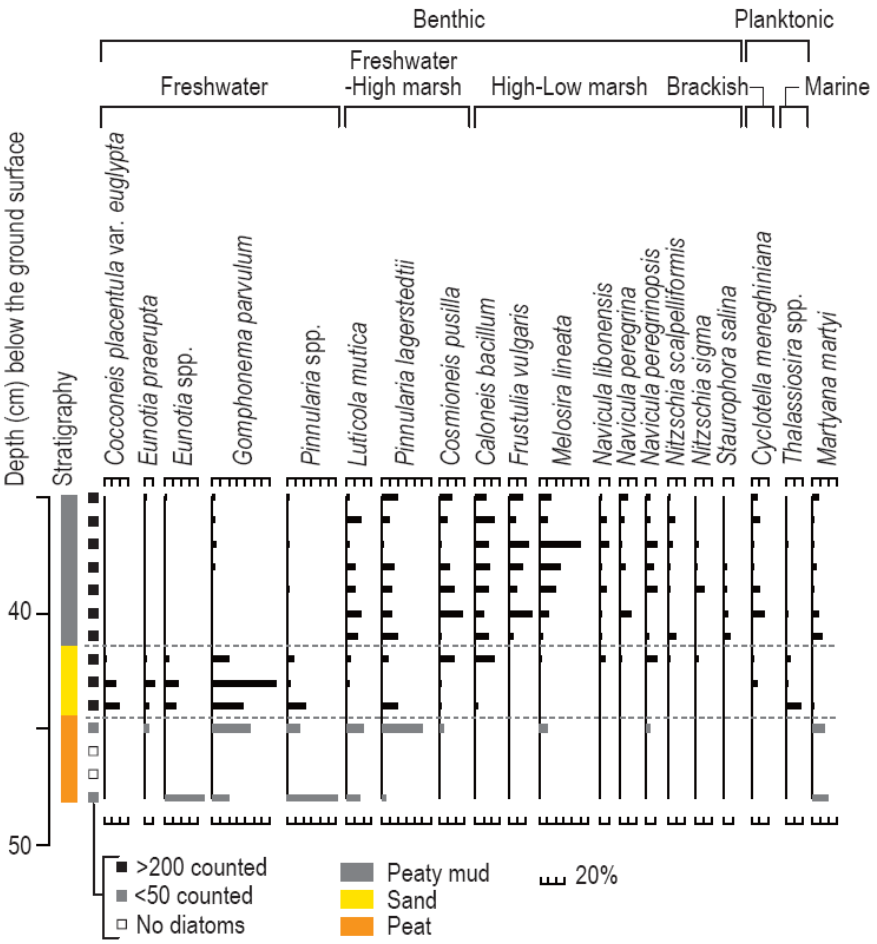

Figure 10 Diatom assemblages present in 1700 Cascadia tsunami deposit, underlying peat and overlying peaty mud. The change in assemblage from predominantly freshwater species in the peat to diatoms that inhabit high-to-low salt marshes implies that an earthquake subsided the soil prior to sand deposition by the tsunami.

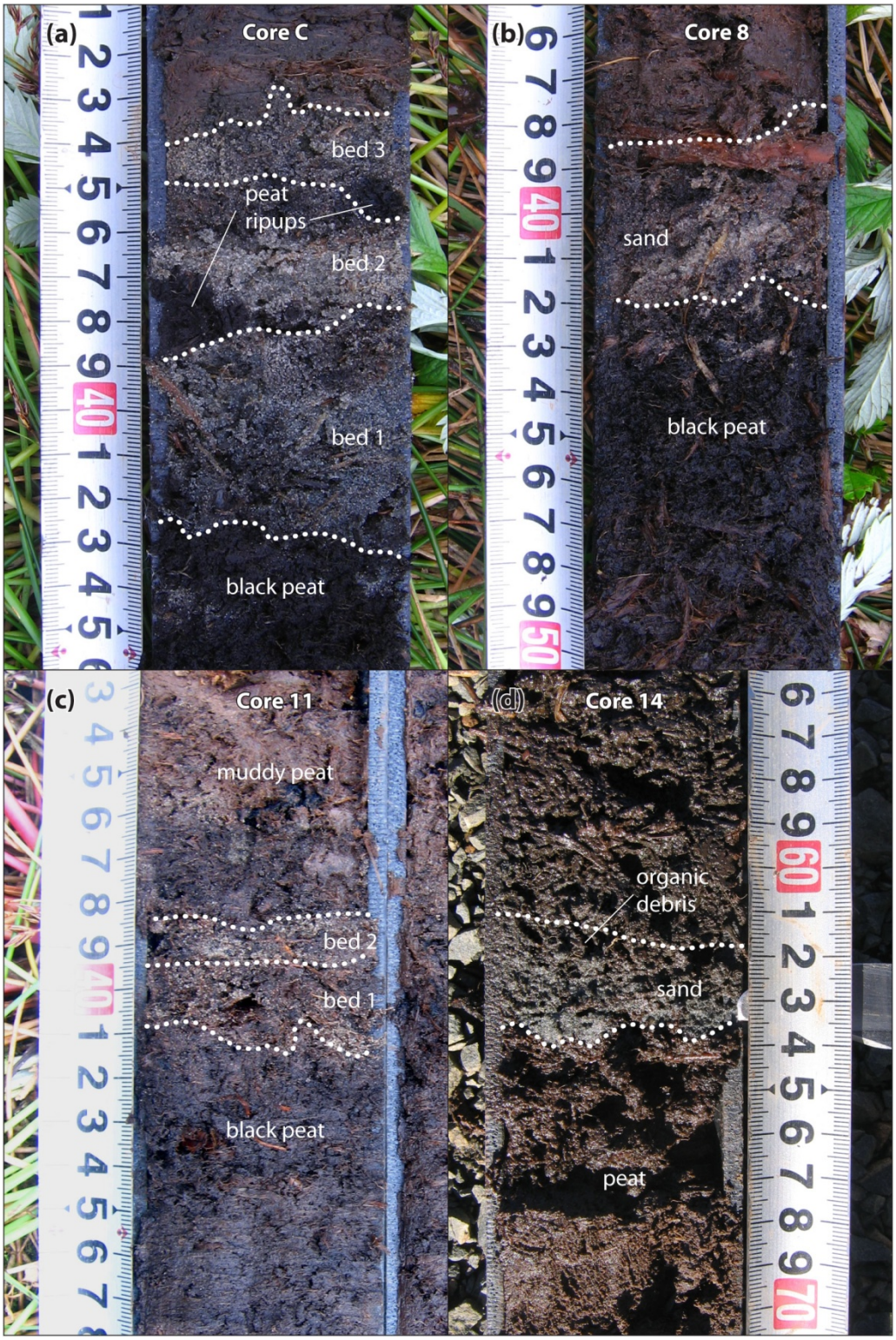

Figure 11 Photographs showing sand layers deposited by the 1700 Cascadia tsunami. (a) Core C; (b) Core 8; (c) Core 11; and (d) Core 14.

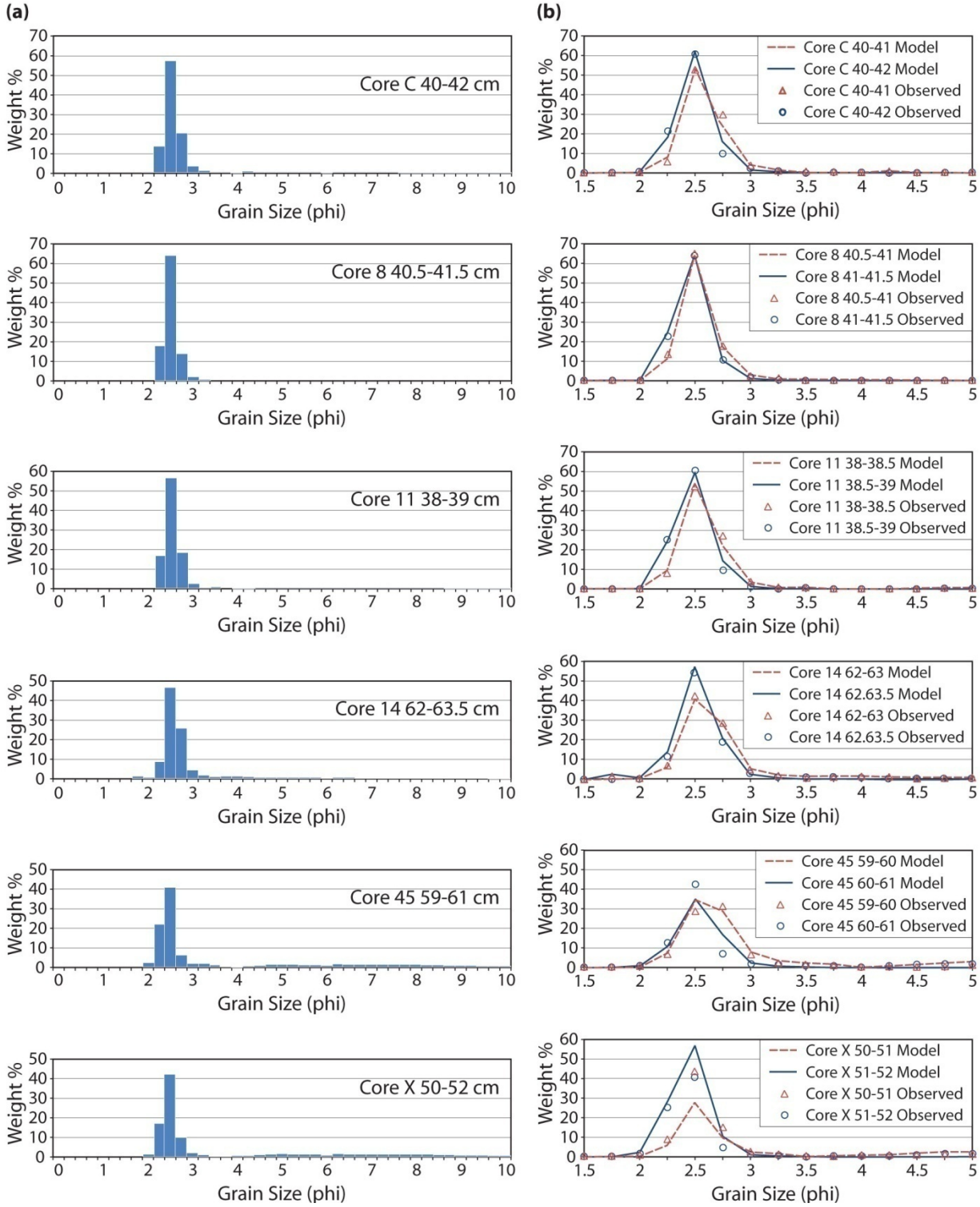

Figure 12 Grain size analyses for selected sand layers from six core sites in the lower Ecola Creek valley. (a) Bulk grain size distributions for multiple sand layers used as model inputs. (b) Comparison of sand particle size distribution measured in the lab (open symbols) to grain size distributions calculated by TsuSedMod (lines). Good matches between data suggest the sand layers settled from suspension.

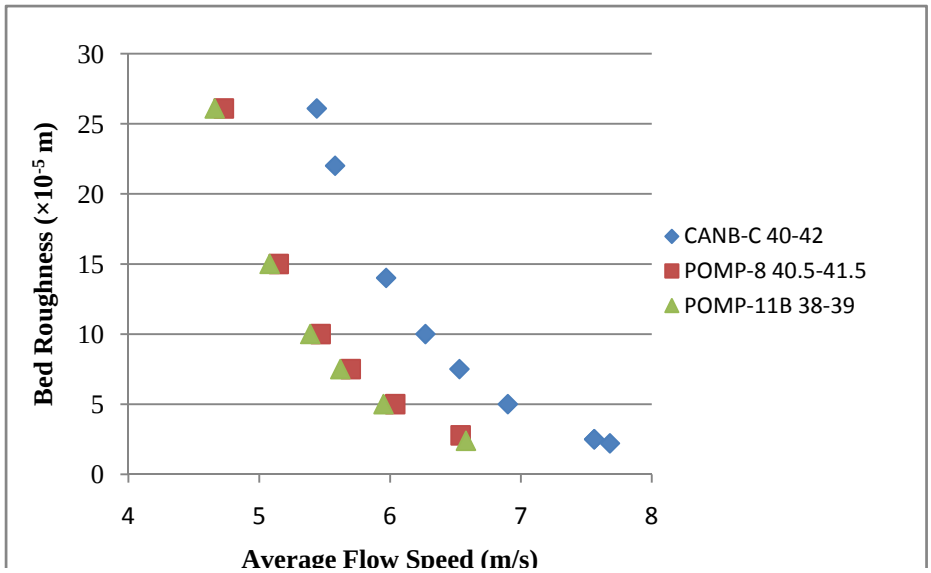

Figure 13 Variations in average flow speed versus bed roughness for cores C, 8 and 11. Model runs use a 5 m flow depth parameter.

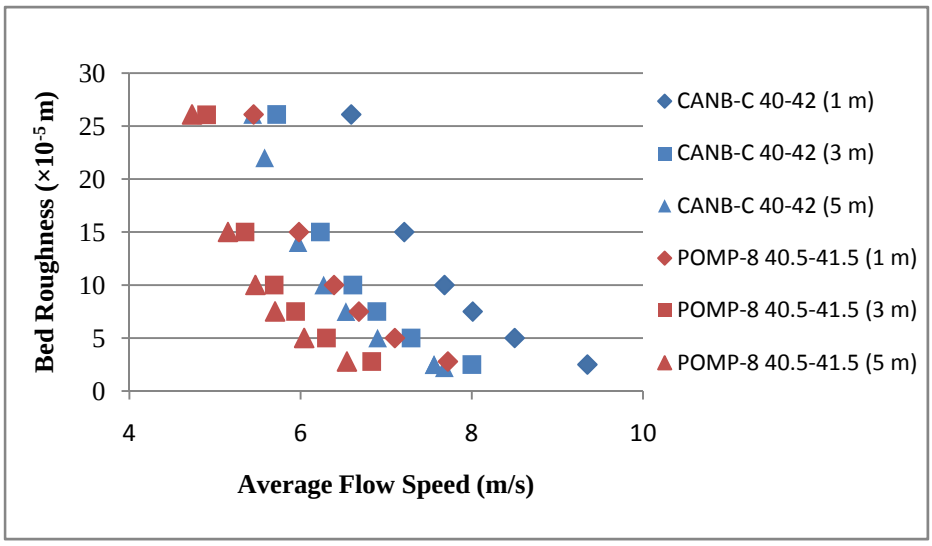

Figure 14 Variations in average flow speed versus bed roughness for cores C and 8, sample interval 40-42 cm related to varying the water depths parameter from 1 to 5 m.

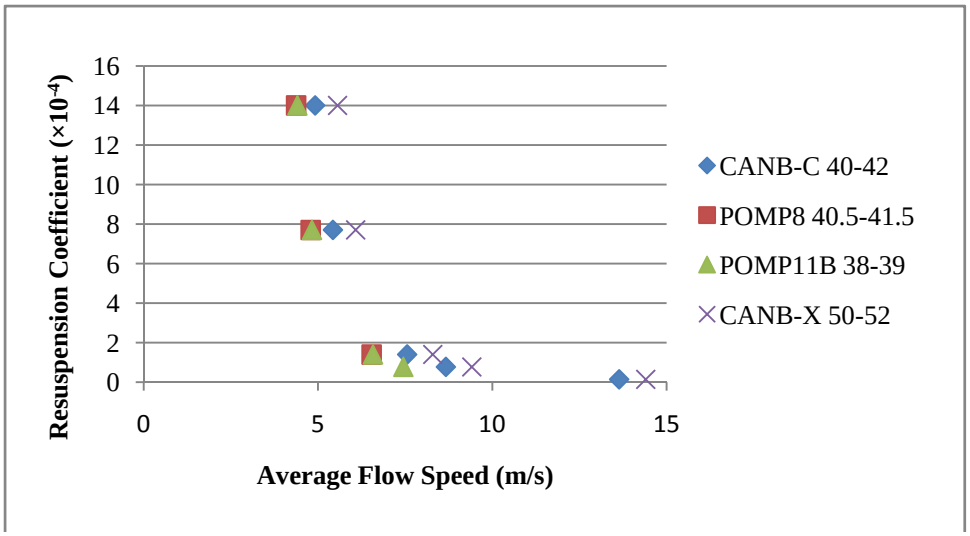

Figure 15 Average flow speed versus resuspension coefficient model parameter.

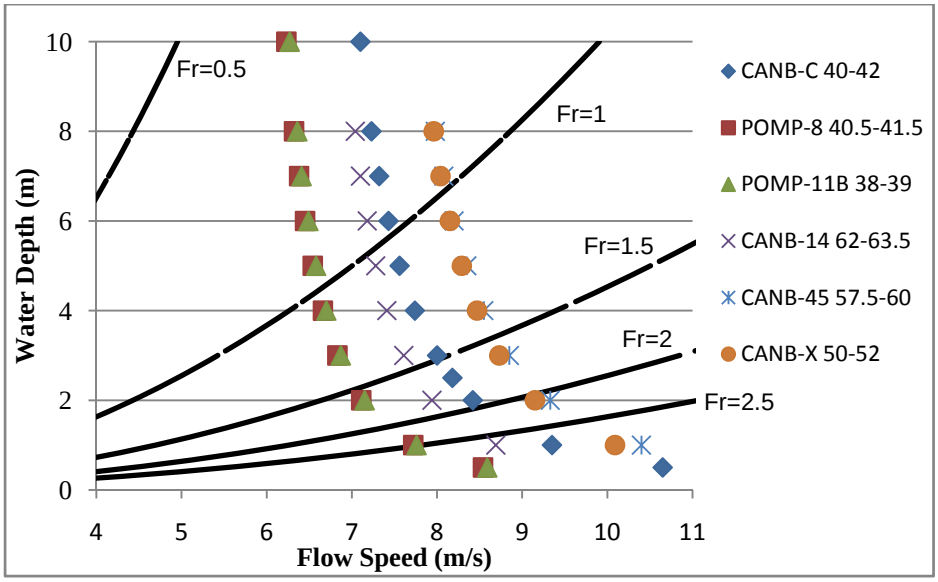

Figure 16 Relations between average flow speed and water depth for model runs of six sand samples. The model varies the roughness parameter to account for roughness created by saltating sediment.

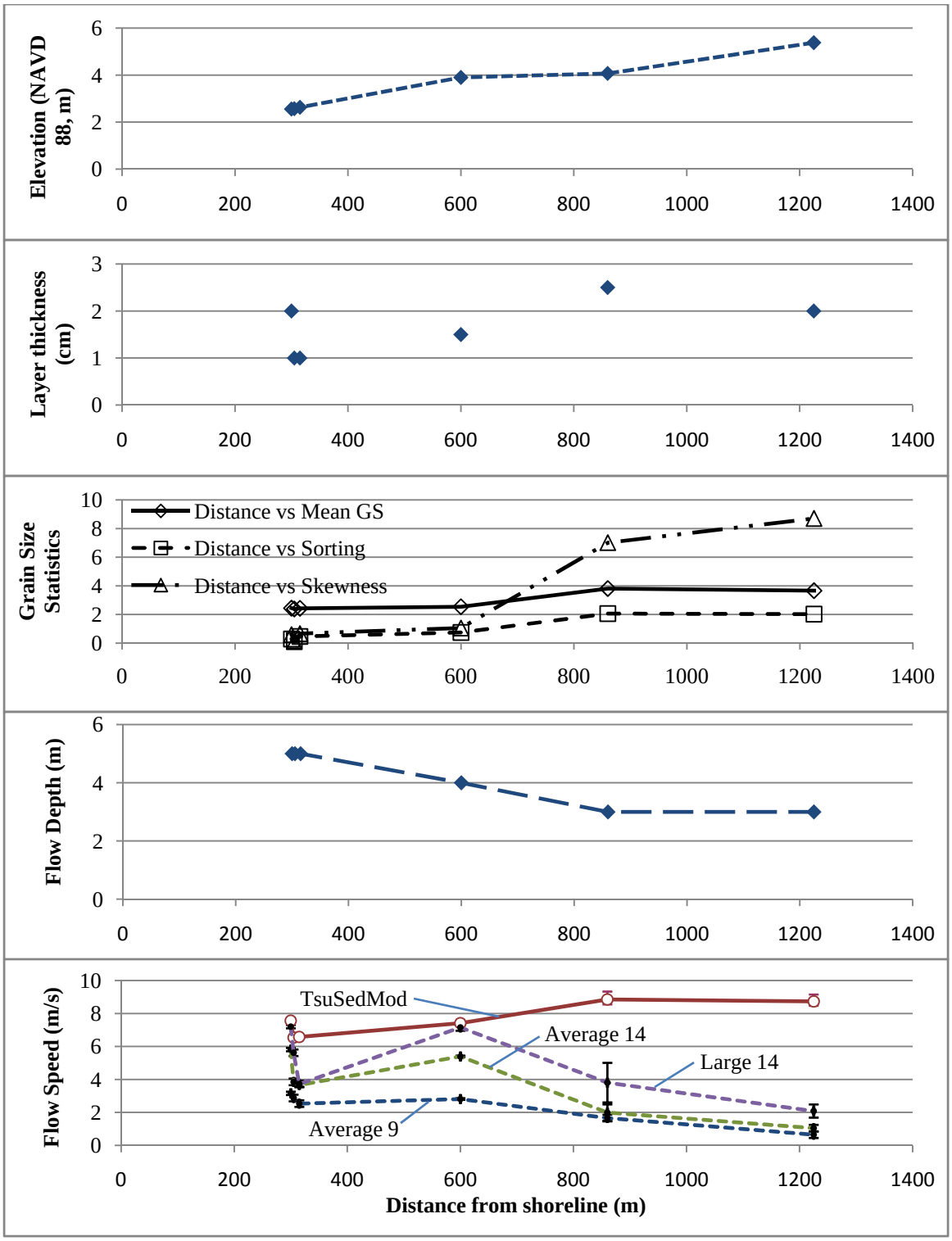

Figure 17 Maximum tsunami flow speed calculated by sediment transport modeling versus numerical simulations of tsunami inundation. Red line shows flow speed calculated by TsuSedMod for sand layers at Cannon Beach. Error bars represent range of flow speeds for runs using flow depths of ±1 m. Dashed lines show maximum velocities predicted by three tsunami simulations for Cannon Beach (Priest et al., 2008).

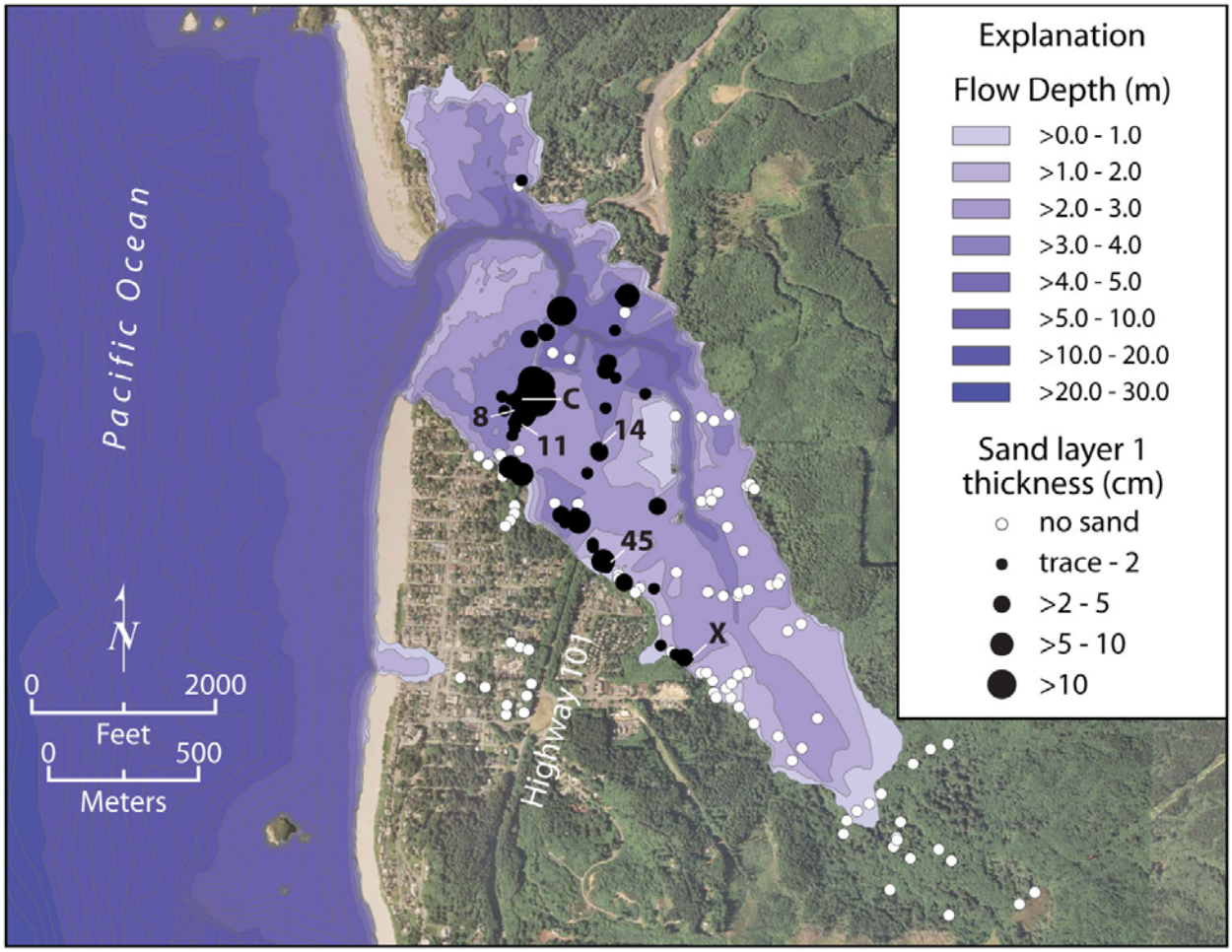

Figure 18 Tsunami flow depths for Cannon Beach tsunami simulation using earthquake model "Average 9." The simulation uses a digital elevation model that reconstructs a 1000-year old prehistoric landscape derived from geologic information. Numbers and letters designate core site locations sampled for tsunami sediment analyses.

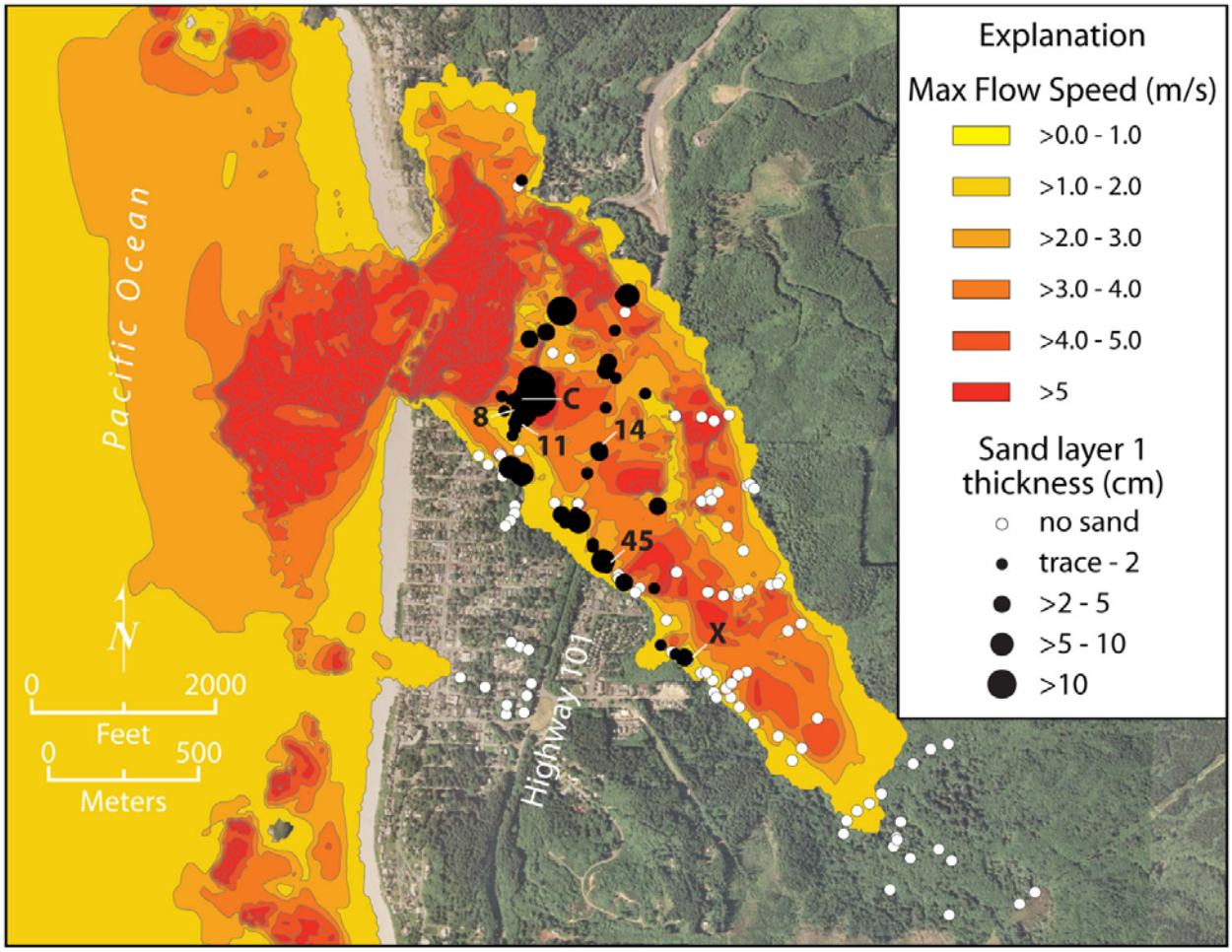

Figure 19 Maximum tsunami flow speed for Cannon Beach tsunami simulation using earthquake model "Average 9." The simulation uses a digital elevation model that reconstructs a 1000-year old prehistoric landscape derived from geologic information. Numbers and letters designate core site locations sampled for tsunami sediment analyses.

APPENDIX A

GRAIN SIZE ANALYSES OF 1700 CASCADIA TSUNAMI DEPOSIT,

CANNON BEACH, OREGON

Location	Cannon Beach	Cannon Beach	Cannon Beach	Cannon Beach	Cannon Beach	Cannon Beach	Cannon Beach	Cannon Beach
Site	Pompey Marsh	Pompey Marsh	Pompey Marsh	Pompey Marsh	Pompey Marsh	Pompey Marsh	Pompey Marsh	Pompey Marsh
Chief Sci	R Witter	R Witter	R Witter	R Witter	R Witter	R Witter	R Witter	R Witter
Core ID	CANB-C	CANB-C	CANB-C	CANB-C	CANB-C	CANB-C	CANB-C	CANB-C
Core Interval	33-34	34-35	36-36.5	36.5-37	38-39	39-40	40-41	41-42
Depth Midpoint	33.5	34.5	36.25	36.75	38.5	39.5	40.5	41.5
Total Weight	6.325819	4.940952	4.781	5.490599	4.132923	5.887	6.154	3.759
Phi Bin	Bin %	Bin %	Bin %	Bin %	Bin %	Bin %	Bin %	Bin %
-1.00	0.00	0.00	0.00	0.00	0.00	0.00	0.00	0.00
-0.75	0.00	0.68	0.00	0.00	0.00	0.00	0.00	0.00
-0.50	0.00	0.00	0.00	0.00	0.00	0.00	0.00	0.00
-0.25	0.00	0.00	0.00	0.00	0.00	0.00	0.00	0.00
0.00	0.00	0.00	0.00	0.00	0.00	0.00	0.00	0.00
0.25	0.00	0.00	0.00	0.00	0.00	0.00	0.00	0.00
0.50	0.00	0.00	0.00	0.00	0.00	0.00	0.00	0.00
0.75	0.00	0.00	0.00	0.00	0.00	0.00	0.00	0.00
1.00	0.00	0.00	0.00	0.00	0.00	0.00	0.00	0.00
1.25	0.00	0.00	0.00	0.00	0.00	0.00	0.00	0.00
1.50	0.00	0.00	0.00	0.00	0.00	0.00	0.00	0.00
1.75	0.00	0.00	0.00	0.00	0.00	0.00	0.00	0.00
2.00	0.76	0.00	0.88	0.00	1.76	0.00	0.00	0.58
2.25	23.17	8.74	30.09	11.50	24.05	11.02	5.67	21.44
2.50	58.54	52.61	58.91	61.42	55.72	57.22	53.00	60.95
2.75	10.58	29.02	6.96	21.42	7.80	22.81	30.05	9.90
3.00	1.72	4.47	0.59	2.56	1.49	3.26	3.94	2.21
3.25	0.00	1.55	0.59	0.88	1.02	1.05	1.15	1.06
3.50	0.00	0.00	0.00	0.00	0.00	0.48	0.67	0.00
3.75	0.00	0.00	0.00	0.00	0.00	0.00	0.67	0.00
4.00	0.58	0.00	0.00	0.50	1.10	0.01	0.05	0.14
4.25	0.04	0.02	0.01	0.04	0.27	0.06	0.98	0.22
4.50	0.14	0.10	0.05	0.08	0.48	0.12	0.17	0.26
4.75	0.22	0.17	0.10	0.10	0.56	0.14	0.19	0.25
5.00	0.23	0.18	0.10	0.09	0.54	0.15	0.20	0.25
5.25	0.21	0.15	0.09	0.08	0.51	0.14	0.20	0.23
5.50	0.20	0.13	0.08	0.08	0.46	0.15	0.19	0.21
5.75	0.21	0.14	0.09	0.08	0.41	0.16	0.19	0.19
5.91	0.14	0.09	0.06	0.05	0.24	0.11	0.13	0.12
6.25	0.29	0.20	0.14	0.11	0.46	0.25	0.27	0.24
6.50	0.22	0.15	0.10	0.08	0.31	0.21	0.20	0.17
6.75	0.23	0.15	0.11	0.08	0.29	0.22	0.20	0.17
7.00	0.23	0.15	0.11	0.08	0.27	0.23	0.20	0.17
7.25	0.23	0.14	0.11	0.08	0.26	0.23	0.20	0.15
7.50	0.23	0.14	0.10	0.08	0.25	0.23	0.19	0.15
7.75	0.22	0.13	0.10	0.07	0.22	0.22	0.17	0.13
8.00	0.21	0.12	0.09	0.07	0.21	0.20	0.16	0.12
8.25	0.19	0.11	0.08	0.06	0.19	0.19	0.14	0.11
8.50	0.17	0.10	0.07	0.06	0.16	0.16	0.12	0.09
8.75	0.15	0.09	0.06	0.05	0.15	0.15	0.11	0.08
9.00	0.14	0.08	0.06	0.04	0.14	0.13	0.10	0.07
9.25	0.13	0.07	0.05	0.04	0.12	0.12	0.09	0.07
9.50	0.12	0.06	0.05	0.04	0.11	0.11	0.08	0.05
9.75	0.11	0.06	0.04	0.03	0.10	0.10	0.07	0.05
9.99	0.10	0.05	0.04	0.03	0.09	0.09	0.06	0.04
10.22	0.08	0.04	0.03	0.03	0.07	0.07	0.05	0.03
10.50	0.09	0.04	0.03	0.03	0.07	0.08	0.06	0.03
10.73	0.06	0.03	0.02	0.02	0.05	0.05	0.03	0.02
10.99	0.05	0.02	0.02	0.01	0.04	0.04	0.03	0.02
11.25	0.02	0.01	0.01	0.01	0.01	0.02	0.01	0.01
11.48	0.00	0.00	0.00	0.00	0.01	0.00	0.00	0.00
11.75	0.00	0.00	0.00	0.00	0.00	0.00	0.00	0.00
12.02	0.00	0.00	0.00	0.00	0.00	0.00	0.00	0.00

Core ID	CANB-C	CANB-C	CANB-C	CANB-C	CANB-C	CANB-C	CANB-C	CANB-C
Core Interval	33-34	34-35	36-36.5	36.5-37	38-39	39-40	40-41	41-42
% Gravel	0	0	0	0	0	0	0	0
% Sand	95.33979	97.066253	98.013246	98.280324	92.939997	95.852854	95.200463	96.283001
% Silt	3.247191	2.161933	1.426411	1.276737	5.739509	2.823722	3.832117	3.026523
% Clay	1.413019	0.771815	0.560343	0.442939	1.320494	1.323424	0.96742	0.690476
% Mud	4.66021	2.933747	1.986754	1.719676	7.060003	4.147146	4.799537	3.716999
Gravel/Sand	0	0	0	0	0	0	0	0
Sand/Silt	29.361	44.898	68.713	76.978	16.193	33.946	24.843	31.813
Silt/Clay	2.298	2.801	2.546	2.882	4.346	2.134	3.961	4.383
Sand/Clay	67.472	125.764	174.917	221.882	70.383	72.428	98.407	139.444
Sand/Mud	20.458	33.086	49.333	57.15	13.164	23.113	19.835	25.903
Gravel/Mud	0	0	0	0	0	0	0	0
F-W Median	2.399443	2.539887	2.352132	2.517567	2.391186	2.519597	2.59077	2.411322
F-W Mean	2.634001	2.522889	2.657338	2.481821	2.492485	2.499936	2.583821	2.669781
F-W Sorting	-0.185193	0.334206	-0.137053	0.314503	0.456805	0.374143	0.323584	-0.10424
F-W Skewness	-0.666026	-0.312725	0.727682	-0.47605	2.608784	-0.238028	0.106349	1.490823
F-W Kurtosis	-0.905275	3.859419	-0.181229	4.593315	6.123734	4.302109	9.715992	0.403482
F-W Kurtosis	-0.905275	3.859419	-0.181229	4.593315	6.123734	4.302109	9.715992	0.403482
Inman Mean	2.75128	2.51439	2.809941	2.463947	2.543135	2.490106	2.580347	2.799011
Inman Sorting	-0.217885	0.174126	-0.326107	0.163566	0.034975	0.18203	0.130525	-0.273413
Inman Skew 16-84	-1.614782	-0.146428	-1.403864	-0.327819	4.344451	-0.162013	-0.079856	-1.417958
Inman Skew 05-95	0.326513	-2.243651	-0.752273	-2.931122	36.19102	-1.611923	1.910681	-1.724027
Inman Kurtosis	0.15486	3.683816	-1.263103	3.695192	40.450321	4.13281	5.531028	-1.39186
Trask Median	0.189538	0.171956	0.195856	0.174637	0.190626	0.174392	0.165997	0.187983
Trask Mean	0.19388	0.174125	0.160837	0.18263	0.191556	0.179026	0.16497	0.192684
Trask Sorting	1.082162	1.06187	0.87416	1.048642	1.069566	1.063638	1.025237	1.078351
Trask Skewness	1.039851	1.021694	0.662312	1.091168	1.005226	1.049858	0.987046	1.044684
Trask Kurtosis	-0.549538	0.175515	0.478044	0.084174	0.267163	0.118384	0.072816	-0.305298
Mean Phi	2.57527	2.569267	2.412718	2.502755	2.637908	2.634352	2.669471	2.513367
Mean mm	0.16779	0.16849	0.187802	0.176439	0.160661	0.161058	0.157184	0.175146
Variance	1.174905	0.761149	0.515118	0.419531	1.315587	1.063065	0.882663	0.720065
Std. Dev.	1.08393	0.872439	0.717717	0.647712	1.14699	1.031051	0.939501	0.848566
Skewness	4.907381	4.890635	7.435361	7.794996	4.085912	5.141702	5.179092	5.718501
Kurtosis	28.137952	38.5542	64.176693	73.627453	20.870586	30.716895	32.627796	39.444513

Location	Cannon Beach	Cannon Beach	Cannon Beach	Cannon Beach
Site	Pompey Marsh	Pompey Marsh	Pompey Marsh	Pompey Marsh
Chief Sci	R Witter	R Witter	R Witter	R Witter
Core ID	Pomp-8	Pomp-8	Pomp-8	Pomp-8
Core Interval (cm)	41-41.5	40.5-41	39.5-40.5	38.5-39.5
Depth Midpoint	41.25	40.75	40	39
Total Weight				
Phi Bin	Bin %	Bin %	Bin %	Bin %
-1	0	0	0	0
0	0	0	0	0
0.25	0	0	0	0
0.5	0	0	0	0
0.75	0	0	0	0
1	0	0	0	0
1.25	0	0	0	0
1.5	0	0	0	0
1.75	0	0	0	0
2	0	0	1.26	0
2.25	22.41	13.04	26.62	12.06
2.5	63.5	64.43	61.19	55.69
2.75	10.37	17.26	6.49	23.94
3	1.57	2.26	0	3.67
3.25	0	1.08	0.68	1.16
3.5	0	0	0.58	0
3.75	0	0	0	0
4	0.07	0.03	0	0
4.25	0.07	0.05	0.02	0.02
4.5	0.09	0.07	0.11	0.09
4.75	0.1	0.08	0.19	0.17
5	0.12	0.08	0.2	0.19
5.25	0.12	0.08	0.16	0.17
5.5	0.11	0.08	0.14	0.15
5.75	0.1	0.08	0.15	0.16
6	0.06	0.05	0.1	0.11
6.25	0.13	0.11	0.2	0.23
6.5	0.1	0.08	0.15	0.17
6.75	0.1	0.09	0.15	0.17
7	0.1	0.09	0.15	0.18
7.25	0.1	0.09	0.15	0.18
7.5	0.09	0.09	0.15	0.18
7.75	0.08	0.08	0.14	0.17
8	0.08	0.08	0.13	0.16
8.25	0.07	0.08	0.12	0.15
8.5	0.06	0.07	0.11	0.13
8.75	0.06	0.06	0.1	0.12
9	0.05	0.06	0.09	0.1
9.25	0.05	0.05	0.08	0.09
9.5	0.04	0.05	0.08	0.09
9.75	0.04	0.05	0.07	0.08
10	0.03	0.04	0.06	0.06
10.25	0.03	0.03	0.04	0.05
10.5	0.03	0.03	0.05	0.05
10.75	0.02	0.02	0.03	0.03
11	0.02	0.02	0.03	0.02
11.25	0.02	0.02	0.02	0.01
11.5	0.01	0.01	0.01	0
11.75	0.01	0.01	0.01	0
12	0.01	0	0.01	0
14	0.01	0.01	0	0

Core ID	Pomp-8	Pomp-8	Pomp-8	Pomp-8
Core Interval (cm)	41-41.5	40.5-41	39.5-40.5	38.5-39.5
% Gravel	0	0	0	0
% Sand	97.91	98.1	96.81	96.52
% Silt	1.54	1.3	2.27	2.48
% Clay	0.54	0.6	0.92	1
% Mud	2.09	1.9	3.19	3.48
Gravel/Sand	0	0	0	0
Sand/Silt	63.42	75.51	42.67	38.9
Silt/Clay	2.84	2.15	2.47	2.47
Sand/Clay	180.21	162.6	105.45	96.15
Sand/Mud	46.91	51.56	30.38	27.7
Gravel/Mud	0	0	0	0
F-W Median	2.27	2.43	2.34	2.48
F-W Mean	2.31	2.43	2.3	2.43
F-W Sorting	0.17	0.18	0.17	0.19
F-W Skewness	0.36	0.02	-0.17	-0.2
F-W Kurtosis	1.71	1.55	4.01	1.57
Inman Median	2.27	2.43	2.34	2.48
Inman Mean	2.33	2.43	2.28	2.41
Inman Sorting	0.15	0.16	0.14	0.12
Inman Skew 1	0.43	0.02	-0.46	-0.53
Inman Skew 2	0.59	0.03	0.3	0.43
Inman Kurtosis	0.97	1.06	1.5	2.41
Trask Median	0.21	0.19	0.2	0.18
Trask Mean	0.2	0.19	0.21	0.18
Trask Sorting	1.05	1.06	1.02	1.08
Trask Skewness	0.91	1.03	1.12	1.02
Trask Kurtosis	0.15	0.25	0.08	0.23
Mean Phi (1st Mo	2.45	2.5	2.48	2.59
Variance	0.51	0.51	0.8	0.84
Std. Dev.	0.72	0.72	0.9	0.92
Skewness (2nd M	7.68	7.76	6.08	5.66
Kurtosis (3rd Mor	69.86	70.89	43.21	37.39

Location	Cannon Beach	Cannon Beach	Cannon Beach	Cannon Beach	Cannon Beach
Site	Pompey Marsh	Pompey Marsh	Pompey Marsh	Pompey Marsh	Pompey Marsh
Chief Sci	R Witter	R Witter	R Witter	R Witter	R Witter
Core ID	POMP-11B	POMP-11B	POMP-11B	POMP-11B	POMP-11B
Core Interval (cm)	40-40.5	39-40	38.5-39	38-38.5	37-38
Depth Midpoint	40.25	39.5	38.75	38.25	37.5
Total Weight					
Phi Bin	Bin %	Bin %	Bin %	Bin %	Bin %
-1	0	0	0	0	0
0	0	0	0	0	0
0.25	0	0	0	0	0
0.5	0	0	0	0	0
0.75	0	0	0	0	0
1	0	0	0	0	0
1.25	0	0	0	0	0
1.5	0	0	0	0	0
1.75	0	0	0	0	0
2	0	0	0	0	0
2.25	15.01	10	25.13	8.18	23.58
2.5	48.74	53.9	60.6	52.4	53.84
2.75	12.32	25.24	9.47	27.04	7.46
3	1.58	4.19	0.97	3.72	0.87
3.25	0.71	1.14	0	0.93	0.52
3.5	0.63	0.76	0.48	0.65	0.43
3.75	0	0	0	0	0
4	0.07	0.01	0	0.01	0.03
4.25	0.52	0.11	0.02	0.1	0.25
4.5	1.41	0.33	0.12	0.28	0.73
4.75	2	0.45	0.21	0.39	0.97
5	2.12	0.41	0.22	0.39	0.93
5.25	2	0.35	0.19	0.35	0.8
5.5	1.83	0.3	0.17	0.34	0.76
5.75	1.62	0.27	0.17	0.36	0.73
6	0.92	0.16	0.11	0.23	0.45
6.25	1.64	0.29	0.22	0.45	0.86
6.5	1.01	0.19	0.16	0.33	0.61
6.75	0.86	0.18	0.16	0.33	0.59
7	0.76	0.18	0.15	0.33	0.57
7.25	0.65	0.17	0.15	0.33	0.55
7.5	0.55	0.16	0.15	0.33	0.52
7.75	0.48	0.15	0.14	0.3	0.49
8	0.4	0.14	0.13	0.29	0.45
8.25	0.36	0.13	0.12	0.27	0.43
8.5	0.27	0.11	0.1	0.24	0.37
8.75	0.25	0.1	0.1	0.22	0.33
9	0.21	0.1	0.08	0.2	0.29
9.25	0.19	0.08	0.08	0.18	0.27
9.5	0.15	0.07	0.07	0.16	0.24
9.75	0.15	0.07	0.06	0.15	0.21
10	0.11	0.05	0.05	0.12	0.17
10.25	0.11	0.04	0.04	0.1	0.13
10.5	0.11	0.04	0.04	0.1	0.16
10.75	0.06	0.03	0.03	0.06	0.09
11	0.06	0.03	0.02	0.06	0.09
11.25	0.04	0.02	0.02	0.04	0.07
11.5	0.04	0.01	0.01	0.02	0.04
11.75	0.02	0.01	0.01	0.02	0.04
12	0.02	0	0.01	0.01	0.03
14	0.04	0.01	0.01	0.01	0.04

Core ID	POMP-11B	POMP-11B	POMP-11B	POMP-11B	POMP-11B
Core Interval (cm)	40-40.5	39-40	38.5-39	38-38.5	37-38
% Gravel	0	0	0	0	0
% Sand	79.06	95.25	96.65	92.92	86.72
% Silt	18.75	3.84	2.49	5.12	10.27
% Clay	2.18	0.92	0.86	1.96	3.01
% Mud	20.94	4.75	3.35	7.08	13.28
Gravel/Sand	0	0	0	0	0
Sand/Silt	4.22	24.81	38.82	18.16	8.44
Silt/Clay	8.58	4.2	2.89	2.6	3.42
Sand/Clay	36.19	104.07	112.19	47.29	28.83
Sand/Mud	3.78	20.03	28.84	13.12	6.53
Gravel/Mud	0	0	0	0	0
F-W Median	2.41	2.44	2.35	2.45	2.37
F-W Mean	3.18	2.45	2.33	2.48	2.39
F-W Sorting	1.36	0.27	0.18	0.6	0.87
F-W Skewness	0.87	0.35	-0.05	0.57	0.5
F-W Kurtosis	5.06	2.45	1.83	7.46	9.78
Inman Median	2.41	2.44	2.35	2.45	2.37
Inman Mean	3.56	2.46	2.32	2.49	2.4
Inman Sorting	1.31	0.15	0.16	0.14	0.23
Inman Skew 1	0.88	0.17	-0.21	0.31	0.12
Inman Skew 2	1.53	2.3	0.21	10.3	9.34
Inman Kurtosis	0.79	3.41	1.1	11.4	9.73
Trask Median	0.19	0.18	0.2	0.18	0.19
Trask Mean	0.18	0.18	0.2	0.17	0.2
Trask Sorting	1.14	1.08	1.05	1.07	1.07
Trask Skewness	0.91	0.91	1.06	0.89	1.02
Trask Kurtosis	0.12	0.21	0.15	0.17	0.07
Mean Phi (1st Mo	3.15	2.64	2.5	2.78	2.91
Variance	2.65	0.89	0.79	1.58	2.59
Std. Dev.	1.63	0.94	0.89	1.26	1.61
Skewness (2nd M	2.17	5.2	6.03	4.04	2.89
Kurtosis (3rd Mor	7.5	33.59	42.93	19.79	11.04

Location	Cannon Beach	Cannon Beach	Cannon Beach	Cannon Beach	Cannon Beach
Site	Pompey Marsh	Pompey Marsh	Pompey Marsh	Pompey Marsh	Pompey Marsh
Chief Sci	R Witter	R Witter	R Witter	R Witter	R Witter
Core ID	CANB-14	CANB-14	CANB-14	CANB-14	CANB-14
Core Interval	63.5-64	63-63.5	62-63	61-62	60-61
Depth midpoint	63.75	63.25	62.5	61.5	60.5
Total Weight	2.713	2.93665	2.588281	1.606687	1.15
Phi Bin	Bin %	Bin %	Bin %	Bin %	Bin %
-1	0	0	0	0	0
-0.75	0	0	0	0	0
-0.5	0	0	0	0	0
-0.25	0	0	0	0	0
0	0	0	0	0	0
0.25	0	0	0	0	0
0.5	0	0	0	0	0
0.75	0	0	0	0	0
1	0	0	0	0	0
1.25	0	0	0	0	0
1.5	0	0	0	0	0.708261
1.75	0	0	1.539065	0	0.786957
2	0	0	0.724266	2.286318	1.495217
2.25	6.625876	11.640586	6.880526	14.534453	7.633478
2.5	48.558202	54.078311	42.279019	46.052985	37.616522
2.75	31.804201	18.88158	28.699034	12.574751	22.664348
3	5.679322	3.024719	5.069861	2.69459	3.934783
3.25	1.514486	0.916582	1.901198	0.408271	1.888696
3.5	0	1.191556	0.814799	1.061505	0.472174
3.75	0	1.191556	1.176932	1.306468	0.472174
4	0.544895	0.777477	1.303883	1.354975	0.606261
4.25	0.183321	0.194365	1.100792	0.9338	0.996261
4.500136	0.265094	0.374549	0.624807	1.142942	1.495565
4.750106	0.265628	0.437947	0.58694	1.155784	1.589304
5	0.245853	0.40875	0.558539	1.137438	1.512609
5.249891	0.235164	0.400409	0.539606	1.0824	1.299565
5.49981	0.245853	0.40875	0.511206	0.990672	1.214348
5.750106	0.245853	0.417092	0.454405	0.917289	1.193043
5.912673	0.160339	0.275281	0.284003	0.568719	0.766957
6.249891	0.331367	0.567245	0.568006	1.119092	1.47
6.49981	0.251198	0.417092	0.407071	0.82556	1.043913
6.750106	0.256543	0.425434	0.397604	0.82556	1.001304
7.000462	0.261887	0.40875	0.397604	0.807214	1.001304
7.249891	0.251198	0.40875	0.378671	0.788868	0.98
7.501116	0.251198	0.392067	0.378671	0.752177	0.916087
7.748554	0.235164	0.358699	0.340804	0.697139	0.852174
7.998616	0.213785	0.342016	0.32187	0.642102	0.745652
8.252088	0.197752	0.308648	0.284003	0.568719	0.63913
8.501116	0.176373	0.266939	0.255603	0.47699	0.532609
8.751659	0.154994	0.241914	0.217736	0.421953	0.426087
9.00231	0.138961	0.216888	0.189335	0.366915	0.383478
9.252088	0.122927	0.183521	0.160935	0.293532	0.34087
9.501116	0.112237	0.175179	0.142002	0.256841	0.276957
9.751659	0.106893	0.158495	0.123068	0.238495	0.276957
9.994931	0.090859	0.125128	0.104134	0.183458	0.213043
10.217323	0.074825	0.108444	0.085201	0.146766	0.170435
10.501116	0.08017	0.116786	0.085201	0.165112	0.170435
10.726997	0.048102	0.066735	0.047334	0.091729	0.085217
10.994931	0.042757	0.058393	0.037867	0.073383	0.085217
11.252088	0.021379	0.025026	0.018934	0.036692	0.034087
11.480357	0.005345	0.008342	0.009467	0.018346	0.008522
11.751659	0	0	0	0	0
12.024678	0	0	0	0	0

Core ID	CANB-14	CANB-14	CANB-14	CANB-14	CANB-14
Core Interval	63.5-64	63-63.5	62-63	61-62	60-61
% Gravel	0	0	0	0	0
% Sand	94.726981	91.701378	90.469287	82.25983	78.278869
% Silt	3.899447	6.237941	7.770086	14.398511	18.078087
% Clay	1.373572	2.060681	1.760628	3.341659	3.643044
% Mud	5.273019	8.298622	9.530713	17.74017	21.721131
Gravel/Sand	0	0	0	0	0
Sand/Silt	24.292	14.701	11.643	5.713	4.33
Silt/Clay	2.839	3.027	4.413	4.309	4.962
Sand/Clay	68.964	44.501	51.385	24.616	21.487
Sand/Mud	17.964	11.05	9.492	4.637	3.604
Gravel/Mud	0	0	0	0	0
F-W Median	2.541577	2.508265	2.510808	2.47519	2.519522
F-W Mean	2.559401	2.516432	2.604485	3.057607	3.293892
F-W Sorting	0.473954	0.849172	0.685758	1.33701	1.492457
F-W Skewness	0.27551	0.272611	0.687375	0.839815	0.864638
F-W Kurtosis	7.429219	8.425664	6.449764	5.201239	3.875045
F-W Kurtosis	7.429219	8.425664	6.449764	5.201239	3.875045
Inman Mean	2.568312	2.520515	2.651323	3.348815	3.681078
Inman Sorting	0.158531	0.221287	0.284206	1.080891	1.342861
Inman Skew 16-8	0.168644	0.05536	0.494413	0.808245	0.864986
Inman Skew 05-9	3.141564	5.395108	5.557161	2.119156	1.74381
Inman Kurtosis	7.215904	10.013505	5.312543	1.431941	1.017623
Trask Median	0.171755	0.175767	0.175457	0.179843	0.174401
Trask Mean	0.166889	0.176968	0.166448	0.174425	0.153361
Trask Sorting	1.051065	1.08564	1.082224	1.154388	1.219722
Trask Skewness	0.941799	1.006901	0.894347	0.921526	0.74355
Trask Kurtosis	0.127097	0.082708	0.092654	0.131962	0.153705
Mean Phi	2.721026	2.820996	2.870981	3.141987	3.309537
Mean mm	0.151666	0.141513	0.136694	0.113284	0.100863
Variance	1.149902	1.749907	1.626609	2.917443	3.211776
Std. Dev.	1.072335	1.32284	1.275386	1.708052	1.792143
Skewness	4.662041	3.550153	3.376311	2.254904	1.95553
Kurtosis	26.029329	15.728121	15.036653	7.387537	6.011774

Location	Cannon Beach	Cannon Beach	Cannon Beach	Cannon Beach	Cannon Beach	Cannon Beach	Cannon Beach	Cannon Beach
Site	Ecola Valley	Ecola Valley	Ecola Valley	Ecola Valley	Ecola Valley	Ecola Valley	Ecola Valley	Ecola Valley
Chief Sci	R Witter	R Witter	R Witter	R Witter	R Witter	R Witter	R Witter	R Witter
Core ID	CANB-45	CANB-45	CANB-45	CANB-45	CANB-45	CANB-45	CANB-45	CANB-45
Core Interval (cm)	53-54.5	54.5-55.5	55.5-56.5	56.5-57.5	57.5-59	59-60	60-61	61-62
Depth Midpoint	53.75	55	56	57	58.25	59.5	60.5	61.5
Total Weight								
Phi Bin	Bin %	Bin %	Bin %	Bin %	Bin %	Bin %	Bin %	Bin %
-1	0	0	No data	0	0	0	0	0
0	0	0	spilled in lab	0	0	0	0	0
0.25	0	0		0	0	0	0	0
0.5	0	0		0	0	0	0	0
0.75	0	0		0	0	0	0	0
1	0	0		0	0	0	0	0
1.25	0	0		0	0	0	0	0
1.5	0	0		0	0	0	0	0
1.75	0.28	0		0.9	0	0	0	0.82
2	0.28	1.12		2.55	0.46	0.74	3.55	2.01
2.25	3.21	12.4		26.14	6.61	12.51	30.81	7.5
2.5	14.95	30.5		31.8	28.37	42.02	38.57	33.21
2.75	16.7	6.14		3.72	30.75	6.99	5.2	22.51
3	5.38	2.01		1.52	6.38	1.82	1.73	3.79
3.25	2.08	1.4		1.59	2.08	1.55	1.82	1.71
3.5	2.22	1.56		0.76	1.38	0.87	0.91	1.56
3.75	2.08	0.73		0	0.85	0.74	0	1.19
4	0.01	0		0	0	0.18	0	0
4.25	0.23	0.12		0.01	0	0.8	0.01	0.02
4.5	1.32	0.9		0.28	0.06	1.52	0.16	0.34
4.75	2.47	1.97		1.15	0.49	1.75	0.65	1.09
5	2.69	2.31		1.82	1.14	1.61	1	1.53
5.25	2.22	1.99		1.71	1.3	1.47	0.96	1.39
5.5	2.06	1.72		1.4	1.09	1.41	0.75	1.11
5.75	2.22	1.81		1.3	0.92	1.38	0.7	1.08
6	1.53	1.28		0.93	0.62	0.92	0.5	0.77
6.25	3.17	2.65		1.99	1.48	1.83	1.11	1.65
6.5	2.43	2.03		1.58	1.18	1.44	0.85	1.31
6.75	2.59	2.21		1.61	1.25	1.51	0.92	1.36
7	2.69	2.34		1.68	1.32	1.61	0.96	1.39
7.25	2.85	2.38		1.68	1.32	1.61	0.96	1.41
7.5	2.91	2.47		1.71	1.32	1.64	0.96	1.39
7.75	2.85	2.34		1.58	1.25	1.57	0.92	1.31
8	2.69	2.3		1.52	1.18	1.51	0.87	1.26
8.25	2.54	2.12		1.4	1.09	1.38	0.8	1.13
8.5	2.22	1.85		1.27	0.97	1.21	0.71	1
8.75	2.01	1.68		1.09	0.88	1.08	0.63	0.9
9	1.74	1.46		0.96	0.76	0.95	0.56	0.77
9.25	1.48	1.24		0.84	0.65	0.82	0.47	0.64
9.5	1.32	1.1		0.71	0.58	0.69	0.38	0.57
9.75	1.16	0.97		0.62	0.49	0.62	0.35	0.49
10	0.95	0.79		0.5	0.39	0.52	0.26	0.39
10.25	0.69	0.62		0.37	0.3	0.36	0.21	0.28
10.5	0.74	0.62		0.4	0.3	0.43	0.21	0.31
10.75	0.48	0.4		0.22	0.21	0.26	0.12	0.21
11	0.37	0.31		0.22	0.16	0.23	0.12	0.18
11.25	0.16	0.13		0.16	0.14	0.16	0.09	0.13
11.5	0.05	0.04		0.12	0.07	0.1	0.05	0.08
11.75	0	0		0.09	0.07	0.1	0.05	0.08
12	0	0		0.03	0.05	0.03	0.03	0.05
14	0	0		0.09	0.12	0.07	0.09	0.1

Core ID	CANB-45	CANB-45	CANB-45	CANB-45	CANB-45	CANB-45	CANB-45	CANB-45
Core Interval (cm)	53-54.5	54.5-55.5	55.5-56.5	56.5-57.5	57.5-59	59-60	60-61	61-62
% Gravel	0	0		0	0	0	0	0
% Sand	47.17	55.87		68.98	76.88	67.42	82.59	74.3
% Silt	36.92	30.8		21.93	15.91	23.57	12.28	18.4
% Clay	15.9	13.33		9.09	7.21	9.01	5.14	7.3
% Mud	52.83	44.13		31.02	23.12	32.58	17.41	25.7
Gravel/Sand	0	0		0	0	0	0	0
Sand/Silt	1.28	1.81		3.15	4.83	2.86	6.73	4.04
Silt/Clay	2.32	2.31		2.41	2.21	2.62	2.39	2.52
Sand/Clay	2.97	4.19		7.59	10.66	7.48	16.08	10.18
Sand/Mud	0.89	1.27		2.22	3.33	2.07	4.74	2.89
Gravel/Mud	0				0	0	0	0
F-W Median	4.65	2.74		2.41	2.52	2.43	2.35	2.57
F-W Mean	5.03	4.24		3.82	3.73	3.87	3.12	3.77
F-W Sorting	2.46	2.45		2.23	1.93	2.18	1.61	1.98
F-W Skewness	0.27	0.82		0.89	0.91	0.91	0.86	0.87
F-W Kurtosis	0.63	0.65		0.86	3.21	0.9	6.5	1.2
Inman Median	4.65	2.74		2.41	2.52	2.43	2.35	2.57
Inman Mean	5.22	4.99		4.53	4.33	4.58	3.51	4.36
Inman Sorting	2.77	2.72		2.41	1.93	2.32	1.4	2.03
Inman Skew 1	0.21	0.83		0.88	0.94	0.93	0.82	0.88
Inman Skew 2	0.44	1.08		1.26	1.47	1.31	1.92	1.37
Inman Kurtosis	0.29	0.32		0.4	0.65	0.46	1.13	0.58
Trask Median	0.04	0.15		0.19	0.17	0.18	0.2	0.17
Trask Mean	0.09	0.11		0.12	0.14	0.12	0.2	0.11
Trask Sorting	5	4.74		3.06	1.33	2.89	1.14	2.14
Trask Skewness	0.73	0.08		0.14	0.6	0.15	0.98	0.26
Trask Kurtosis	0.45	0.45		0.41	0.2	0.43	0.12	0.35
Mean Phi (1st Mo	4.99	4.49		3.8	3.63	3.88	3.16	3.67
Variance	6.46	6.67		5.88	4.63	5.57	3.9	4.84
Std. Dev.	2.54	2.58		2.42	2.15	2.36	1.97	2.2
Skewness (2nd M	0.48	0.72		1.27	1.73	1.29	2.18	1.59
Kurtosis (3rd Mor	1.87	2.09		3.32	4.83	3.42	6.74	4.39

Location	Cannon Beach	Cannon Beach
Site	Ecola Valley	Ecola Valley
Chief Sci	R Witter	R Witter
Core ID	CANB-X	CANB-X
Core Interval	50-51	51-52
Depth Midpoint	50.5	51.5
Total Weight	3.484949	4.065
Phi Bin	Bin %	Bin %
-1	0	0
-0.75	0	0
-0.5	0	0
-0.25	0	0
0	0	0
0.25	0	0
0.5	0	0
0.75	0	0
1	0	0
1.25	0	0
1.5	0	0
1.75	0	0
2	0.874605	1.63444
2.25	8.746055	25.185241
2.5	43.584505	40.489544
2.75	14.941176	4.531857
3	2.478049	1.188684
3.25	1.239024	0.742927
3.5	0.437303	0
3.75	0	0.520049
4	0.930158	0.005399
4.25	0.80264	0.138562
4.500136	1.149727	0.776359
4.750106	1.252769	1.41647
5	1.22023	1.493592
5.249891	1.193113	1.233948
5.49981	1.165997	1.079705
5.750106	1.111765	1.105412
5.912673	0.759254	0.771218
6.249891	1.545624	1.542435
6.49981	1.193113	1.131119
6.750106	1.247346	1.182534
7.000462	1.328694	1.233948
7.249891	1.328694	1.285363
7.501116	1.355811	1.285363
7.748554	1.301578	1.233948
7.998616	1.22023	1.208241
8.252088	1.165997	1.105412
8.501116	1.0033	0.976876
8.751659	0.894835	0.874047
9.00231	0.813486	0.796925
9.252088	0.705022	0.719803
9.501116	0.650789	0.642681
9.751659	0.56944	0.56556
9.994931	0.460976	0.514145
10.217323	0.379627	0.385609
10.501116	0.406743	0.411316
10.726997	0.21693	0.257073
10.994931	0.21693	0.205658
11.252088	0.081349	0.102829
11.480357	0.027116	0.025707
11.751659	0	0
12.024678	0	0

Core ID	CANB-X	CANB-X
Core Interval	50-51	51-52
% Gravel	0	0
% Sand	73.230485	74.298142
% Silt	19.176865	18.118218
% Clay	7.59265	7.583641
% Mud	26.769515	25.701858
Gravel/Sand	0	0
Sand/Silt	3.819	4.101
Silt/Clay	2.526	2.389
Sand/Clay	9.645	9.797
Sand/Mud	2.736	2.891
Gravel/Mud	0	0
F-W Median	2.511319	2.409399
F-W Mean	3.740602	3.751179
F-W Sorting	1.953058	1.901381
F-W Skewness	0.93602	1.013386
F-W Kurtosis	1.261445	1.204191
F-W Kurtosis	1.261445	1.204191
Inman Mean	4.355244	4.422069
Inman Sorting	2.01466	1.859789
Inman Skew 16-84	0.915254	1.082203
Inman Skew 05-95	1.482153	1.628248
Inman Kurtosis	0.549095	0.7238
Trask Median	0.175395	0.188234
Trask Mean	0.114981	0.119953
Trask Sorting	2.019449	2.130366
Trask Skewness	0.271848	0.240334
Trask Kurtosis	0.341769	0.435749
Mean Phi	3.647499	3.528512
Mean mm	0.079798	0.086659
Variance	4.824811	5.020704
Std. Dev.	2.196545	2.240693
Skewness	1.554054	1.587741
Kurtosis	4.122356	4.198175